



저작자표시-비영리-변경금지 2.0 대한민국

이용자는 아래의 조건을 따르는 경우에 한하여 자유롭게

- 이 저작물을 복제, 배포, 전송, 전시, 공연 및 방송할 수 있습니다.

다음과 같은 조건을 따라야 합니다:



저작자표시. 귀하는 원저작자를 표시하여야 합니다.



비영리. 귀하는 이 저작물을 영리 목적으로 이용할 수 없습니다.



변경금지. 귀하는 이 저작물을 개작, 변형 또는 가공할 수 없습니다.

- 귀하는, 이 저작물의 재이용이나 배포의 경우, 이 저작물에 적용된 이용허락조건을 명확하게 나타내어야 합니다.
- 저작권자로부터 별도의 허가를 받으면 이러한 조건들은 적용되지 않습니다.

저작권법에 따른 이용자의 권리는 위의 내용에 의하여 영향을 받지 않습니다.

이것은 [이용허락규약\(Legal Code\)](#)을 이해하기 쉽게 요약한 것입니다.

[Disclaimer](#)

공학석사학위논문

**A Study on Optimal Array Configuration
of Tidal Stream Turbine Farm based on
Actuator Disc Modeling**

액츄에이터 디스크 모델에 기반한
조류발전단지 형상 최적화에 관한 연구

2019년 2월

서울대학교 대학원

건설환경공학부

한 지 수

ABSTRACT

A Study on Optimal Array Configuration of Tidal Stream Turbine Farm based on Actuator Disc Modeling

Han, Jisu

Department of Civil & Environmental Engineering

Graduate School of Seoul National University

Tidal current energy is a sustainable and predictable renewable energy resource. In tidal farm design, optimization of array configuration is essential as tidal farm is constituted of hundreds of turbines. This study aimed to suggest a generalized optimal array configuration for idealized tidal straits. Due to the strong nonlinear interaction between tidal device and tidal flow, optimizing two-dimensional array position should base on PDE-constrained gradient-based optimization algorithm. PDE is given as two-dimensional nonlinear steady shallow water equation in order to reflect the movement of tidal flow and reduce computational cost. Total power output is the target functional to be maximized, and OpenTidalFarm is used as a tool for coupling PDE solver and optimization algorithm. Turbine was parameterized as an actuator disc. Optimization was undertaken with various situations, such as varying number of deployed turbines N , minimum distance

constraint d_{\min} , spanwise farm site constraint L_y and initial conditions. It was found that optimization result is highly dependent on d_{\min} and L_y , and also sensitive to initial condition. Thus, it is recommended to use proper initial condition which resembles optimal array configurations. Analysis on the various case of optimized result (over 100 cases) suggests that linear barrage with uniform spacing can be considered as acceptable optimal array. Furthermore, if linear barrage shape is impossible due to the optimization constraints (such as d_{\min} and L_y), it was observed that connecting all turbines as a curved or V shaped barrage performs better than splitting the array into two parts. This study highlights the necessity of designing proper site constraints and distance constraints, showing that the performance of optimal array for identical N can vary up to 50% with different constraints. It is expected that this optimal shape of array can be implemented for array design in tidal energy resource assessment or for recommended initial condition in gradient-based optimization.

Keywords: Tidal array configuration, Gradient-based Optimization, Steady shallow water equation, Actuator Disc, OpenTidalFarm.

Student Number: 2017-23008

Table of Contents

ABSTRACT	i
Table of Contents	iii
List of Figures	vi
List of Tables.....	viii
Nomenclature	ix
Chapter 1. Introduction	1
1.1 Tidal current energy and its assessment.....	1
1.2 Tidal farm optimization	4
1.3 Necessity of defining generalized configuration of decent tidal array.....	5
1.4 Aim of the thesis	6
1.4.1 Modeling tidal turbine in 2D Shallow Water using Actuator Disc modeling...	7
1.4.2 Finding optimal array configuration via PDE-constrained gradient-based optimization	7
1.4.3 Analyzing the relationship between optimization constraints and optimization results.....	8
Chapter 2. Theoretical background.....	9
2.1 Linear Momentum Actuator Disc Theory (LMADT).....	9
2.1.3 Betz’s unbounded flow	11
2.3.2 Garrett and Cummins’s rigid lid flow.....	14
2.3.3 Houlsby et al.’s free-surface flow	18
2.3.4 Limitations of LMADT.....	24
2.2 Shallow Water Equation (SWE)	25
2.3 PDE-constrained Gradient-based Optimization using Adjoint method	27
2.3.1 Gradient-based Optimization	28

Chapter 3. Methodology	30
3.1 Specifications of OpenTidalFarm	30
3.1.1 Design Parameters.....	30
3.1.2 PDE constraint	31
3.1.3 Turbine Parameterisation	31
3.1.4 Target functional.....	32
3.1.5 Box and inequality constraints.....	33
3.1.6 Gradient-based optimization with adjoint approach	34
3.2 Realistic Actuator Disc Modeling in 2D SWE	35
3.2.1 Actuator disc modeling in 2D SWE and 3D flow model.....	36
3.2.2 Wake properties behind tidal turbine	37
3.2.3 Simulation settings for tuning K and ν	38
3.2.4 Simulation results.....	44
3.3 Pilot Test 1: effect of initial condition and number of turbines on optimization result.....	46
3.3.1 Simulation settings	46
3.3.2 Simulation results.....	49
3.3.3 Conclusions of pilot test 1.....	49
3.4 Pilot Test 2: effect of minimum distance constraint and spanwise length of the farm site on optimization result	50
3.4.1 Simulation settings.....	50
3.4.2 Simulation results.....	52
3.4.3 Conclusions of pilot test 2.....	55
3.5 Main test: maximum number of turbines which can be considered as a barrage type configuration	56
3.5.1 Simulation settings	56
Chapter 4. Results and Discussions	60
4.1 Analysis on optimal array configuration and tidal farm output	60
4.2 Extracted Power and N_{\max}	64
4.3 Limitations of the Modeling	65

Chapter 5. Conclusions	68
APPENDIXS.....	71
Appendix A.....	71
Appendix B.....	73
Appendix C.....	78
REFERENCES	86
국문초록.....	91

List of Figures

Figure 1 Types of tidal turbine. Horizontal, vertical, duct type, from left to right. Adopted from Adcock et al. [1].	2
Figure 2 Schematic figure of LMADT in unbounded flow	12
Figure 3 Schematic figure of LMADT in rigid lid flow	14
Figure 4 Schematic figure of LMADT in free-surface flow	19
Figure 5 Blockage ratio of array of turbine fully expanded to the channel width.	20
Figure 6 Solution of Equation 2.32 versus α_4 . Solid line is for case $B = 0.64, Fr = 0.14$ and dashed line is for case $B = 0.2, Fr = 0.3$	22
Figure 7 Effect of C_T on C_P by varying the blockage ratio B . Fr is fixed as 0.09	23
Figure 8 Flow chart of gradient-based optimization.....	27
Figure 9 Smoothed friction function with $K=1, x=10, y=10$ and $r=5$	32
Figure 10 (Left) Schematic drawing of 3D actuator disc modeling. a) Plane view is identical to 2D actuator disc modeling, b) disc area is partially spanning the water depth. (Right) Schematic drawing of 2D actuator disc modeling in SWE. a) Plane view is identical to 2D actuator disc modeling, b) disc area is fully spanning the water depth.	36
Figure 11 Schematic representation of simulation domain for single turbine tuning , pilot test 2 and main test.	39
Figure 12 Schematic representation of simulation domain for optimization.....	40
Figure 13 (Left) velocity field and (Right) pressure field with selected K and ν	45
Figure 14 Normalized velocity along downstream wake by upstream velocity, U_{init} . . 45	45
Figure 15 Schematic representation of simulation domain for pilot test 1	47

Figure 16 Concept description of LHS.....	49
Figure 17 Mesh domain and farm constraint used in pilot test 2 and main test.	51
Figure 18 Value of (Nd_{\min}/L_Y) for 20 subcases in pilot test 2. Specific color indicates the type of optimized array configuration.	53
Figure 19 Optimized results with highest performance. (left) $d_{\min}=2D$ and L3, (center) $d_{\min}=1.5D$ and L5, (right) $d_{\min}=1.5D$ and L4.....	54
Figure 20 Bar chart of averaged individual turbine power (P_i) for 20 subcases of pilot test 2.	55
Figure 21 (left) Schematic figure of arc initial condition. Lowercase r is the radius of curvature, and turbines maintain interspacing of d_{\min} . (right) Part of initial conditions for $L_Y = 230m$ and $d_{\min} = 1.5D$	58
Figure 22 (left) plot of averaged individual turbine power (P_i) for all cases. (right) plot of total farm power output (P_t) for all cases.	60
Figure 23 Velocity magnitude field for (upperleft) N=8 case 1, (upperright) N=9 case 3 and (lowercenter) N=15 case 7.....	63
Figure 24 Trend of averaged individual power (P_i , marked in black) and total generated power (P_t , marked in gray) for each cases.....	65

List of Tables

Table 1 Summarized list of studies on wake properties behind the tidal device.	38
Table 2 Summary of mesh used in single turbine modeling, pilot test 2 and main test.	39
Table 3 Parameter settings for pilot test	44
Table 4 Several specifications of commercial tidal turbines, adopted from Roberts et. al [26].....	44
Table 5 Summary of simulation domain for pilot test 1.	47
Table 6 Summary of C_p for 20 subcases of pilot test 2.....	54
Table 7 Definition of case and its corresponding range of N in the main test. In total 70 cases are optimized.	59
Table 8 List of maximum and minimum power for each number of turbines.	61
Table 9 Optimized configuration for each N , maximum and minimum cases corresponding to table 8.....	62

Nomenclature

LMADT

A	Disc area
$A_{t,i}$	Area of turbine flow at Station i
B	Blockage ratio (Turbine size/cross-sectional area of strait)
C_T	Thrust coefficient, normalized with upstream dynamic pressure
C_{TL}	Local thrust coefficient, normalized with dynamic pressure at station 2
$C_{ P}$	Power coefficient, normalized with upstream kinetic flux
D	Disc diameter
Fr	Froude number
T	Thrust exerted on fluid
P	Power available from disc
g	Gravitational acceleration
α_i	Velocity coefficient of turbine flow at Station i , normalized with upstream velocity
β_i	Velocity coefficient of bypass flow at Station I , normalized with upstream velocity
ρ	Density of water

Optimization

A	Turbine area
D	Turbine diameter
H	Still water depth
K_i	Friction coefficient of i^{th} turbine
N	Number of optimized turbines
T	Tidal period
d_{\min}	Minimum inter-turbine distance
h	Water depth
g	Gravitational acceleration
m	Design parameter
p_i	Coordinate vector of i^{th} turbine
r	Turbine radius
x_i	x coordinate of i^{th} turbine
y_i	y coordinate of i^{th} turbine
Δ	Grid size of unstructured grid
ϕ_0	Phase lag in tidal range
ρ	Density of water
η	Water elevation
ν	Kinematic viscosity

Chapter 1. Introduction

1.1 Tidal current energy and its assessment

As a sustainable and predictable renewable energy resource, status of tidal energy has arisen and research is ongoing actively [16]. Gravity force between the earth, moon and sun generates tide-generating force which therefore can be predicted with precision for a long future. This is a particular advantage in comparison to other point-time renewable energy resources such as wind and solar power energy [1].

There exist two categories in tidal energy technologies: tidal barrage and tidal current [1]. Tidal barrage technology generates power from height difference between ebb and flood by constructing barrage, resulting concerns about their environmental impact in ocean. Hence, interest on tidal current technology has considerably increased in both research field and industry since mid-2000's [26]. Tidal current or tidal stream technologies extract kinetic energy of tidal current in a similar mechanism to wind turbines. Horizontal and vertical axis turbines are major turbine type in practical usage, and furthermore can be enclosed within a duct.

Estimating potential tidal resource is essential for designing governmental plan for renewable energy supply and deciding productive target site. Naïve version of tidal energy assessment method is calculating undisturbed kinetic flux of coastal site, using depth averaged velocity of coastal site. However, this is criticized by excessively overestimating

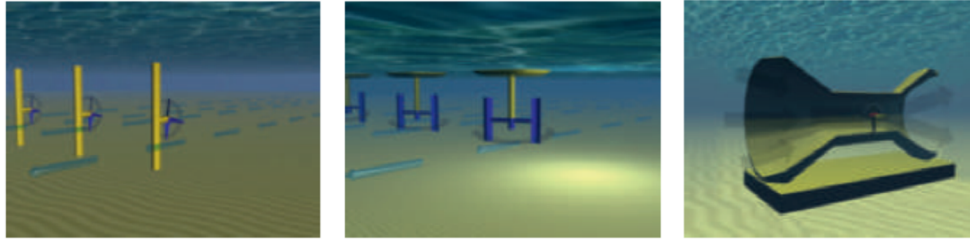


Figure 1 Types of tidal turbine. Horizontal, vertical, duct type, from left to right. Adopted from Adcock et al. [1].

the energy potential by ignoring the feedback effect of energy extraction on tidal currents [30]. Garrett and Cummins was the first who proposed response model of channel to existence of tidal turbine using 1D shallow water equation [10]. When hydraulic drag induced from tidal turbine is significant, volume flux through the channel reduces further reducing the tidal farm's energy extraction. This was succeeded by Vennell [32, 33] and Gupta and Young [13] with improved turbine modeling methods. In the aforementioned cases, turbine array was assumed to be a linear tidal fence and its impact was modeled as thrust proportional to velocity square.

Local impact of energy extraction can be modeled using Linear momentum actuator disc theory, which is well known theory in aerodynamics. LMADT simplify turbine as actuator disc with same side of turbine. When momentum is extracted from the disc, changes in local flow is related to the extracted power and its relationship is derived using conservation of mass, momentum and energy. Garrett and Cummins extended unbounded LMADT into open-channel problem simplifying problem by fixing the water level restrict on low Fr problem, and showed that power is proportional to $(1-B)^{-2}$ where B denotes ratio of turbine blocking the channel [12]. Houlsby et al. extended it further by considering free-surface change [16].

One of the common assumption used for turbine modeling theories mentioned before is the uniform interspacing between turbine devices where the array expands the whole channel width (fully-spanned). In practical situations, however, it is plausible that tidal array is constrained due to economic reasons or need to assure passage for marine life and vessels. Nishino and Willden was the first to introduce the concept of ‘scale separation’ and it enabled to expand rigid-lid LMADT for cases where array partially blocks the channel width (partially-spanned) [23]. Partially-spanned LMADT for free-surface flow is further derived by Vogel et. al [35].

Past researches have validated fully-spanned LMADT both numerically and experimentally [22, 14, 29, 5, 31], and LMADT have been widely applied as in real-site ocean modeling for tidal energy resource assessments. Realistic upper-limit of tidal stream power potential was obtained with advanced turbine modeling including its hydrodynamics. In addition, LMADT itself can be utilized as a tool of rough estimation of maximum power potential for idealized tidal straight, returning the changes in the tidal flow properties (velocity and water depth). However, to conclude that energy resource assessment via LMADT is the maximum power available, it should be verified that the configuration used in the model is optimal. LMADT assumes the array is deployed as a shape of linear barrage with periodically implemented identical turbines inside. Bonar et. al showed that linear barrage type array yields maximum power output when turbines are identical and uniformly spaced [2]. To my best knowledge, yet there is no research questioning that placing array as a fully-spanned (or partially-spanned if site is constrained) linear barrage gives the maximum power output. Thus, optimal array configuration should

be analyzed for idealized condition, where LMADT is derived from; if linear barrage shape is not optimal, correction factor should be used to redress the power upper-limit after maximum power is derived from LMADT.

1.2 Tidal farm optimization

Optimization of renewable energy farm is essential for increasing efficiency and maximizing the available power from total array. This is crucial for determining economic feasibility of farming project, especially when the size of farming is large in order of hundreds of turbines. Due to its longer history of wind energy development, optimization algorithms for wind farm are well-discussed in numerous studies. Wind farm optimization are based on gradient-free algorithm in general. Genetic algorithms are known to yield good results [27], and similar method called particle swarm optimization performed better than genetic algorithms in several researches [19, 36].

While majority of wind farm optimization uses gradient-free algorithms, this cannot be simply followed up in tidal farm for several reasons. First, direction and magnitude of wind is inherently stochastic but tidal flow is predictable and strongly governed by hydrodynamic governing equations. Therefore, genetic algorithm is a good choice considering the randomness of wind, but solving governing equations with genetic algorithm which are PDEs in general would cost significant computational cost. Wind farm design uses simple wake model such as Park wake model since randomness overrides interaction between wind turbines, which is opposite in case of tidal farm because tidal flow is confined. Second, wind turbine effect on upstream is negligible compare to tidal

turbine, making tidal farm optimization problem even more complex [10].

To capture nonlinear flow interactions between turbines, finding numerical solution of PDE and calculate power output is necessary. In this kind of PDE-involving problem, also referred as PDE-constrained optimization, optimization parameter is updated with respect to gradient of target functional which are function of solutions of PDE. Funke et al. proposed efficient gradient-based optimization algorithm and developed an open-source software called OpenTidalFarm[10]. The most recent version involves profit-maximization, taking into account of grid network of tidal farm [6].

However, gradient-based optimization is sensitive to initial condition because calculated maximum or minimum of target functional is local maximum or minimum depending on initial condition. As nonlinearity of equation is strong and number of design parameter increases, target functional becomes extremely complex and dependency of optimization result on initial condition is critical.

1.3 Necessity of defining generalized configuration of decent tidal array

As described in length at the above two subsections, tidal array configuration is critical factor for generated power. There are no general guidelines for designing array of tidal farm, and in previous studies and in-situ test cases generally uses regularly deployed array configuration with enough spacing to ensure less adverse interaction between turbine devices. Acknowledging that is impossible to defining optimal array configuration for all cases due to numerous constraints and variabilities in practical situation, still it is valuable

to study for finding a decent form of array for two reasons. First, the generalized optimal array shape can be implemented in tidal energy assessment and improve the analysis on tidal power resource. In tidal energy assessment, ocean modeling is necessary which's grid dimension is large enough to use idealized turbine modeling derived from ideal conditions. As discussed in chapter 1.1, tidal array is typically assumed to be a linear barrage with uniform spacing. Thorough analysis on decent tidal array would support this kind of assumption or either be a counterpart, suggesting a better shape of array to assess maximum tidal resources. Second, decent array configuration can be implemented in optimization process as initial condition. Since complex high-dimensional nonlinear system contains a myriad of local convex zones, gradient-based optimization easily falls into local optima. Therefore, it is plausible to think that optimization quality will be increased with decent initial condition, yielding an array with guaranteed high performance.

1.4 Aim of the thesis

This thesis is devoted to suggest an optimal array configuration for idealized conditions which can be plausibly considered as efficient and invaluable in an engineering sense. In fact, this decent array cannot be treated as global optima in a mathematical sense, which will largely dependent on the bathymetry and constraints. Nevertheless, generalized optimal array configuration can still be considered as a practically optimal array and provide valuable insights for further design in detail. This research targets three specific objectives to reach the research aim.

1.4.1 Modeling tidal turbine in 2D Shallow Water using Actuator Disc modeling

Computing flow field with tidal turbine is one of the most critical and influential part in this study because velocity field is required for evaluation of tidal farm's performance. Optimized result (i.e. power output and array configuration) will be largely affected by the quality of obtained velocity field and turbine model, thus turbine should be carefully modeled. In order to resolve realistic flow field with modeled tidal turbines, concept of actuator disc is applied and implemented in 2D Shallow Water Equation (SWE). Actuator disc modeling assumes tidal turbine as a penetrable disc which generates pressure drop on the disc and subsequently exert thrust on the fluid body. To understand hydrodynamics of tidal flow with actuator disc is implemented inside, thorough research on Linear Momentum Actuator Disc Theory (LMADT) was conducted. Aftermath, coefficient for actuator model and SWE was tuned to match the properties of wake which were driven from various former researches.

1.4.2 Finding optimal array configuration via PDE-constrained gradient-based optimization

As mentioned in section 1.2, PDE-constrained gradient-based optimization is suitable for optimizing tidal farm array. In this study, an open-source program called OpenTidalFarm is used as a tool to couple finite element based SWE solver and gradient-based optimization. OpenTidalFarm is selected due to its high efficiency for solving PDE and computing functional derivatives. Owing to the inherit drawback of gradient-based optimization, it is hard to ascertain that the optimized result can be regarded as acceptable optima: the generated power from local optimal should not significantly different to actual

global optima. To ensure this, various initial conditions were tested and decent initial condition for optimization was defined.

1.4.3 Analyzing the relationship between optimization constraints and optimization results.

In realistic farm optimization problems, optimization constraints should be applied in order to reflect practical constraints in tidal farm implementation. For example, minimum distance between turbines would be necessary in order to avoid adverse lateral wake effect. In addition, available farm site where turbine can be deployed will be a limited area and act as optimization constraint. In this study, these two optimization constraints were considered as major factor which determines optimal array layout. Relationship between the constraints and properties of optimal array was analyzed.

Chapter 2. Theoretical background

2.1 Linear Momentum Actuator Disc Theory (LMADT)

Linear Momentum Actuator Disc Theory (LMADT) is a theoretical modeling of turbine to examine available power to extract from surrounding flow. Turbine is represented as a penetrable actuator disc which extracts momentum from the flow passing through the turbine. Since the disc is permeable, there is no discontinuity in velocity but pressure drops at the backside of the disc, resulting resistance force on the fluid. This force can be treated analogous to the thrust of an actual turbine, and further power generated by disc, which is product of thrust and velocity of flow passing through the turbine, can indicate the power capacity of the turbine. Solution strictly requires steady state condition because solution of LMADT is calculated under equilibrium state.

LMADT was first introduced for wind turbine modeling by Lanchester and Betz in the early twentieth century [3]. Betz modeled the flow as inviscid, enabling to separately model the flow passing through the device (denoted as turbine flow) and the flow bypasses the turbine (denoted as bypass flow). Different from the flow of air, tidal current is constrained by gravity due to its high density and thus resulting free-surface which makes it difficult to apply LMADT for wind turbine straight forward onto the case of tidal turbine. The model assumed flow to be quasi-inviscid, where flow is inviscid except for the downstream mixing region. This assumption enables to model flow passing through the device (i.e. turbine flow) and flow bypassing the device (i.e. bypass flow) separately until

pressure is equalized for two flows at near downstream, and mix the two flows together by wake effect at far downstream. Houlsby et. al. (henceforth H08) further extended Garrett and Cummins's model (henceforth GC07) with free-surface modeling, taking in count of water level drop at the far downstream due to energy extraction [12, 16].

LMADT mentioned above model tidal array as a long tidal 'fence' expanding for whole channel width with uniformly deployed turbine devices. In practical tidal farm implementation, this kind of design may be restricted by economic and geological constraints (cost of electrical connection and inadequate bathymetry), apart from the need for conserving paths for vessel operation and marine animals. Partially spanned tidal fence act as an obstacle, exerting the aggregated thrust on each tidal device to the channel flow and forces some part the flow to split as bypassing flow. Nishino and Willden expanded the model to incorporate partially spanned tidal fence by introducing the concept of scale separation [23], and further extended it by applying simple power law for array-flow expansion ratio [24]. Both works of Nishino and Willden were developed with rigid-lid assumption, i.e. water level does not change along the channel. Vogel at. al. enhanced the scale-separated LMADT by free-surface modeling, following the logic of H08 model [35].

However, it should be noted that the actuator disc never includes the mechanism of turbine operation. Rather, LMADT is a tool of energy assessment base on the second law of thermodynamics. LMADT provides solution of flow field and available power only for conditions satisfying entropy. Thus, modeling tidal turbines with LMADT will be proper for estimating energy resource of a tidal farm, but should not be used for investigating wake characteristics of turbines. Tidal current modeling using LMADT would yield similar

flow structures in large scale, but smaller scale should be examined with turbine modeling techniques based on rotation of turbine blades. Also, in reality, two flows cannot be completely separated throughout the inviscid region (from the far upstream to the downstream station which meets pressure equilibrium) due to the momentum diffusion induced by velocity difference in turbine flow and bypass flow. However, 3D RANS actuator disc modeling results shows that numerical modeling gives good agreement with analytical solutions of LMADT [24]. Also, 2D numerical modeling results using Shallow Water Equation indicates that quasi-inviscid assumption can be adequate for tidal channels, which will be discussed in part 4.

2.1.3 Betz's unbounded flow

LMADT in aerodynamics is well known and provided a standard of maximum power available for wind turbine, which is also known as Betz's limit. LMADT considers the idealized flow described in Figure 3. The flow is unbounded and has uniform upstream velocity u and pressure at station 1. Also the flow is assumed to be steady, incompressible and inviscid. Actuator disc of size A is located at between station 2 and station 3. Momentum sink due to the disc is expressed as thrust T exerted on the flow. Stream tube passing through the turbine is denoted as 'turbine flow' and the flow passing by the turbine is denoted as 'bypass flow'. Average velocity of turbine flow at station 2 and 3 is represented as $u_2 = \alpha_2 u$. Decreased pressure in turbine flow at station 2 and 3 recovers to the ambient pressure p at station 4, while velocity further decreases as turbine flow expands to reach the horizontally uniform pressure at station 4. Turbine flow velocity at station 4 is

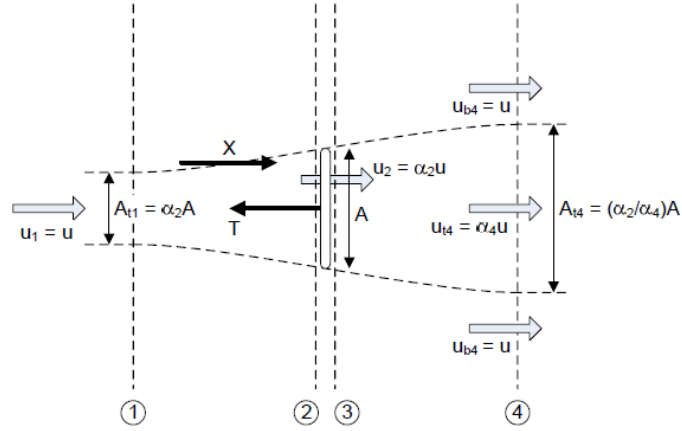


Figure 2 Schematic figure of LMADT in unbounded flow

represented as, $u_4 = \alpha_4 u$ and it is evident that $\alpha_2 > \alpha_4$.

We apply mass, energy and momentum conservation for the turbine flow to derive analytical solution relating the extracted power by the disc to the upstream kinetic flux. To begin, the Bernoulli equation is applied to the turbine flow between station 1 and 2 to give

$$p + \frac{1}{2} \rho u^2 = p_{t,2} + \frac{1}{2} \rho (\alpha_{t,2} u)^2 \quad (2.1)$$

and energy is also conserved in the turbine flow after energy extraction at the disc, between station 3 and 4

$$p_{t,3} + \frac{1}{2} \rho (\alpha_{t,2} u)^2 = p + \frac{1}{2} \rho (\alpha_{t,4} u)^2 \quad (2.2)$$

where the numerical subscripts indicate the averaged quantity at a given station and subscript t indicates turbine flow. Combining Equation 2.1 and 2.2, pressure drop across the disc is

$$\Delta p = p_{t,2} - p_{t,3} = \frac{1}{2} \rho (1 - \alpha_4^2) u^2 \quad (2.3)$$

which is equivalent to the thrust T when multiplied with the disc area A

$$T = \frac{1}{2} \rho A (1 - \alpha_4^2) u^2. \quad (2.4)$$

Thrust can be modeled using momentum flux conservation within turbine flow between station 1 to 4. Net force acting on the control volume equals the change in momentum flux, which gives Equation 2.5

$$\begin{aligned} T &= -\rho A_{t,4} u_4^2 + \rho A_{t,1} u_1^2 \\ &= \rho u^2 A \alpha_2 (1 - \alpha_4) \end{aligned} \quad (2.5)$$

Equation 2.4 and 2.5 are equal, then relationship between coefficient $\alpha_{t,2}$ and $\alpha_{t,4}$ becomes

$$\alpha_2 = \frac{\alpha_4 + 1}{2} \quad (2.6)$$

which implies that the velocity of flow passing through the disc is average of the upstream and downstream flow. Power extracted by disc can be determined as

$$P = T \alpha_2 u = \frac{1}{2} \rho u^3 A \alpha_2 (1 - \alpha_4^2) = \frac{1}{2} \rho u^3 A \frac{(1 - \alpha_4)(1 + \alpha_4)^2}{2} \quad (2.7)$$

which is expressed in terms of one unknown parameter, the downstream velocity coefficient α_4 . We can define the dimensionless thrust coefficient C_T and power coefficient C_p by dividing each with upstream dynamic pressure and upstream kinetic

flux, respectively.

$$C_r = \frac{T}{\frac{1}{2} \rho A u^2} = 1 - \alpha_4^2 \quad (2.8)$$

$$C_p = \frac{P}{\frac{1}{2} \rho A u^3} = \frac{(1 - \alpha_4)(1 + \alpha_4)^2}{2} \quad (2.9)$$

Maximum power coefficient is obtained when $\alpha_4 = 1/3$, which is identical to $\alpha_2 = 2/3$.

Optimal $C_p = 16/27 \approx 0.59$ which is also known as Lanchester-Betz limit. This value gives the upper bound of the power coefficient of wind turbine, which cannot be realized in actual wind turbine due to series of idealization in the LMADT model.

2.3.2 Garrett and Cummins's rigid lid flow

GC07 model follows basic assumptions for the flow conditions: flow is steady and has uniform upstream velocity. Main differences to plug in LMADT into open channel are four

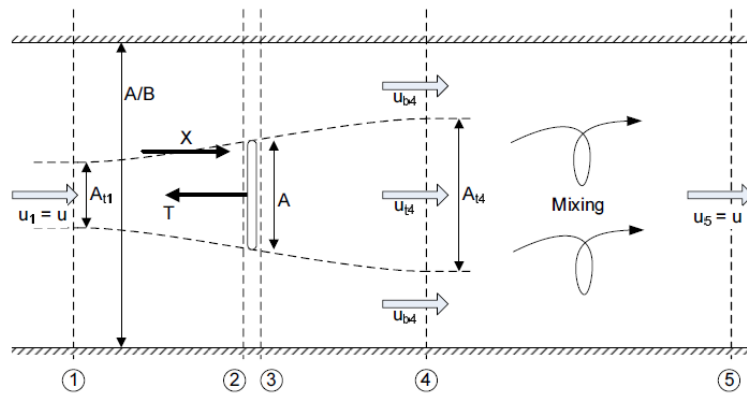


Figure 3 Schematic figure of LMADT in rigid lid flow

points. First, pressure is no longer uniform but hydrostatic at station 1 and 5. Second, channel is assumed to have uniform rectangular cross-section, with rigid lid. To satisfy rigid lid assumption, energy extraction from the flow should not be large enough to deform the free-surface significantly. This can be achieved when the Froude number is very small, i.e. $Fr \ll 1$ [12]. Third, the flow is quasi-inviscid, i.e. viscosity effect is considered only at the mixing zone at the far downstream. Fourth, bed friction and side wall friction is ignored.

As illustrated in Figure 4, conditions from station 1 to 4 are analogous to unbounded LMADT except that the pressure recovers to hydrostatic at station 4. Station 4 is denoted as near-wake region and station 5 is far-wake region. Between station 4 and 5, free-shear turbulence occurs due to the velocity difference of the turbine flow and the bypass flow and velocity becomes uniform at station 5. Since we assumed rigid-lid flow, conservation of mass yields velocity at station 5 recovers to the upstream velocity u . Analogous to previous definitions, bypass velocity at station 4 is expressed as $u_{b,4} = \beta_4 u$.

Velocity of bypass flow increases as the turbine flow expands at the near-wake zone to recover hydrostatic pressure. To ensure continuity of bypass flow between station 1 to 4,

$$u_{b,4} = \frac{1 - B\alpha_2}{1 - B\alpha_2 / \alpha_4} u = \beta_4 u \quad (2.10)$$

where B denotes blockage ratio of the disc versus the channel cross-section. Unlike unbounded scenario, p_4 is no longer same as upstream pressure p . p_4 is obtained by

applying Bernoulli equation at bypass flow within station 1 to 4,

$$p - p_4 = \frac{1}{2} \rho (\beta_4^2 - 1) u^2 = \frac{1}{2} \rho u^2 \left(\left(\frac{1 - B\alpha_2}{1 - B\alpha_2 / \alpha_4} \right)^2 - 1 \right). \quad (2.11)$$

Applying Bernoulli equation either side of the turbine in the turbine flow yields

$$p_{t,2} - p_{t,3} = p - p_4 + \frac{1}{2} \rho u^2 (1 - \alpha_4^2). \quad (2.12)$$

Combining Equation 2.12 with Equation 2.11, we get

$$\Delta p = p_{t,2} - p_{t,3} = \frac{1}{2} \rho u^2 \left(\left(\frac{1 - B\alpha_2}{1 - B\alpha_2 / \alpha_4} \right)^2 - \alpha_4^2 \right) \quad (2.13)$$

which is used to determine the thrust exerted on the flow

$$T = A \Delta p = \frac{1}{2} \rho A u^2 (\beta_4^2 - \alpha_4^2) = \frac{1}{2} \rho A u^2 \left(\left(\frac{1 - B\alpha_2}{1 - B\alpha_2 / \alpha_4} \right)^2 - \alpha_4^2 \right). \quad (2.14)$$

Thrust is also obtained using momentum flux conservation within the control volume from station 1 to 4

$$\begin{aligned} \frac{A}{B} p - \frac{A}{B} p_4 - T &= \rho A_{t,4} u_{t,4}^2 + \rho A_{b,4} u_{b,4}^2 - \frac{A}{B} \rho u^2 \\ &= \rho A u^2 \left(\alpha_2 (\alpha_4 - 1) + \frac{1 - B\alpha_2}{B} \left(\frac{1 - B\alpha_2}{1 - B\alpha_2 / \alpha_4} - 1 \right) \right) \end{aligned} \quad (2.15)$$

which is simplified to

$$p - p_4 = \frac{TB}{A} + \rho u^2 \frac{\alpha_2 B (1 - \alpha_4)^2}{\alpha_4 (1 - B\alpha_2 / \alpha_4)}. \quad (2.16)$$

Combining Equation 2.11 with Equation 2.16, we get

$$B(1-3\alpha_4)\alpha_2^2 + 2\alpha_4^2(1+B)\alpha_2 - \alpha_4^2(1+\alpha_4) = 0 \quad (2.17)$$

which is quadratic equation of α_2 with coefficients are in terms of α_4 and B . For unbounded flow, i.e. $B = 0$, Equation 2.17 reduces to Equation 2.6. For arbitrary B , solution of Equation 2.17 gives

$$\alpha_2 = \frac{1 + \alpha_4}{1 + B + \sqrt{(1-B)^2 + B(1-1/\alpha_4)^2}}. \quad (2.18)$$

Equation 2.18 indicates that turbine flow velocity at the disc is function of B and α_4 , thus from Equation 2.14 thrust is also function of B and α_4 . Power extracted from the disc is

$$P = T\alpha_2 u = \frac{1}{2} \rho A u^3 \alpha_2 \left(\left(\frac{1 - B\alpha_2}{1 - B\alpha_2 / \alpha_4} \right)^2 - \alpha_4^2 \right). \quad (2.19)$$

Non-dimensionalize thrust and power analogous to 2.1.1, we can define C_T and C_P as

$$C_T = \frac{T}{\frac{1}{2} \rho A u^2} = \left(\frac{1 - B\alpha_2}{1 - B\alpha_2 / \alpha_4} \right)^2 - \alpha_4^2 \quad (2.20)$$

$$C_P = \frac{P}{\frac{1}{2} \rho A u^3} = \alpha_2 \left(\left(\frac{1 - B\alpha_2}{1 - B\alpha_2 / \alpha_4} \right)^2 - \alpha_4^2 \right) \quad (2.21)$$

Differentiating C_P respect to α_4 and finding the value of α_4 which makes the differential to zero, C_P is maximized when $\alpha_4 = 1/3$, yielding Equation 2.21 to

$$C_{p,\max} = \frac{16}{27} \left(\frac{1}{1-B} \right)^2 \quad (2.22)$$

which is proportional to the reciprocal of $(1-B)^2$. This result indicates that maximum power available from the disc is increased when the disc blocks higher portion of the channel cross-section. This is the key difference of unbounded flow and confined flow. Energy is extracted not only from kinetic energy, but also from additional pressure drop due to parallel channel wall confining the flow. Later in section 2.1.3, it will be shown that maximum power available is also function of Fr in case of free-surface.

We are interested in the power extraction in this research, so further discussion of power dissipated in the far-wake zone is omitted. Note that rigid-lid assumption gives continuity error in the far downstream since pressure inevitably drops at station 5 due to energy extraction. Continuity error increases as initial flow velocity is fast, i.e. Fr is large, and large amount of energy is extracted due to high blockage ratio.

2.3.3 Housby et al.'s free-surface flow

Extension of LMADT to a flow with variable free-surface elevation is now discussed. The cross-section of tidal channel is again rectangular, with upstream water depth h and uniform channel width b . Blockage ratio B is defined as A/bh . In contrast to rigid-lid case in section 2.1.2, downstream depth at station 4 and 5 are related to energy extraction and downstream flow velocities. This yields LMADT solution to be function of initial water depth h , which is replaced with non-dimensionalized parameter Fr .

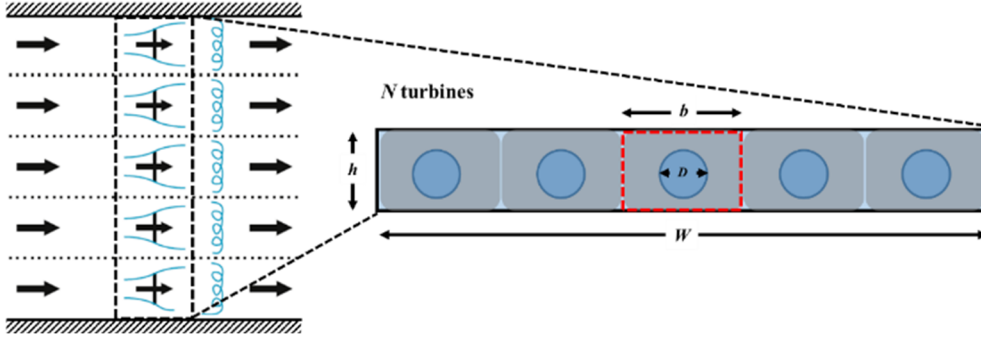


Figure 5 Blockage ratio of array of turbine fully expanded to the channel width.

Using continuity equation at station 1 to 4 for total control volume,

$$h_4 = Bh \frac{\alpha_2}{\alpha_4} + h \frac{(1 - B\alpha_2)}{\beta_4} \quad (2.26)$$

and combining Equation 2.26 with equation 2.23, α_2 is expressed with respect to

B , Fr , α_4 and β_4

$$\alpha_2 = \frac{\alpha_4(\beta_4 - 1)(2 - \beta_4(1 + \beta_4)Fr^2)}{2(\beta_4 - \alpha_4)}. \quad (2.27)$$

Combining equation 2.23, 2.24 and 2.25 gives pressure difference on the disc

$$\Delta p = \rho g(h_{t,2} - h_{t,3}) = \frac{\rho u^2}{2}(\beta_4^2 - \alpha_4^2) \quad (2.28)$$

which gives the thrust when multiplied with disc area A

$$\begin{aligned} T = A\Delta p &= \frac{1}{2} \rho Au^2(\beta_4^2 - \alpha_4^2) \\ &= \frac{1}{2} \rho bhBu^2(\beta_4^2 - \alpha_4^2) \end{aligned} \quad (2.29)$$

Momentum equation in control volume from station 1 to 4 is

$$\begin{aligned}
\frac{1}{2} \rho g b (h^2 - h_4^2) - T &= \rho u^2 A \alpha_2 (\alpha_4 - 1) + \rho u^2 h b (1 - B \alpha_2) (\beta_4 - 1) \\
&= \rho u^2 b h B \alpha_2 (\alpha_4 - 1) + \rho u^2 h b (1 - B \alpha_2) (\beta_4 - 1)
\end{aligned} \tag{2.30}$$

and plug in T as Equation 2.2 into Equation 2.28,

$$\begin{aligned}
\frac{1}{2} g (h^2 - h_4^2) - \frac{1}{2} h B u^2 (\beta_4^2 - \alpha_4^2) \\
= u^2 h B \alpha_2 (\alpha_4 - 1) + u^2 h b (1 - B \alpha_2) (\beta_4 - 1).
\end{aligned} \tag{2.31}$$

After substituting α_2 and h_4 using Equation 2.27 and 2.23 into Equation 2.31, we get

$$\begin{aligned}
\frac{Fr^2}{2} \beta_4^4 + 2\alpha_4 Fr^2 \beta_4^3 - (2 - 2B + Fr^2) \beta_4^2 - (4\alpha_4 + 2\alpha_4 Fr^2 - 4) \beta_4 + \\
\left(\frac{Fr^2}{2} + 4\alpha_4 - 2B\alpha_4^2 - 2 \right) = 0
\end{aligned} \tag{2.32}$$

where its solution gives β_4 as function of three parameters, i.e. $\beta_4 = \beta_4(\alpha_4, B, Fr)$.

Since the Equation 2.32 is quartic in β_4 , its solution is obtained numerically.

Thrust coefficient and power coefficient is

$$C_T = \frac{T}{\frac{1}{2} \rho b h B u^2} = \beta_4^2 - \alpha_4^2 \tag{2.33}$$

$$C_P = \frac{P}{\frac{1}{2} \rho b h B u^3} = \alpha_2 (\beta_4^2 - \alpha_4^2) \tag{2.34}$$

which is same form with rigid-lid case. Difference exist in the equation to obtain

β_4 and α_2 . Later we will need to define thrust and power in terms of local turbine flow $\alpha_2 u$. Then local thrust coefficient and local power coefficient becomes

$$C_{TL} = \frac{T}{\frac{1}{2} \rho b h B (\alpha_2 u)^2} = \frac{\beta_4^2 - \alpha_4^2}{\alpha_2^2} \quad (2.35)$$

$$C_{PL} = \frac{P}{\frac{1}{2} \rho b h B (\alpha_2 u)^3} = \frac{(\beta_4^2 - \alpha_4^2)}{\alpha_2^2} = C_{TL} \quad (2.36)$$

It has been proved numerically that $\alpha_4 = 1/3$ yields maximum power coefficient with respect to α_4 [12]. Also, it should be noted that not all set of parameters result in physically admissible solutions. This is compelling reason since LMADT is a method of calculating extractable power considering the surrounding flow. If the turbine flow becomes excessively slow, bypass flow becomes too fast and its state turns into

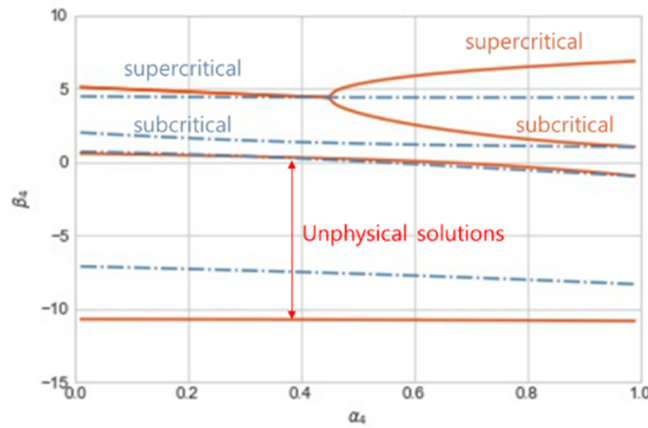


Figure 6 Solution of Equation 2.32 versus α_4 . Solid line is for case $B = 0.64, Fr = 0.14$ and dashed line is for case $B = 0.2, Fr = 0.3$

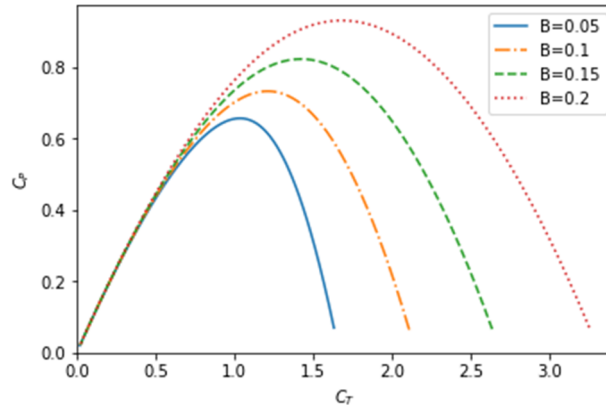


Figure 7 Effect of C_T on C_P by varying the blockage ratio B . Fr is fixed as 0.09 .

supercritical flow. This phenomenon makes the flow more unstable in total, in other words increasing the entropy of total state. It is physically not possible according to the second law of thermodynamics.

Physically inadmissible case is represented as existence of complex solution while solving Equation 2.32. Solution of Equation 2.32 should yield four β_4 s, and since $\beta_4 > 1$ there are two possible solutions to use for further calculation. Open channel flow can have two velocities for one water depth; case of subcritical and supercritical. Therefore, the smaller β_4 denotes subcritical bypass flow and the other one denotes supercritical bypass flow. One should select the subcritical β_4 to determine α_2 and further parameters. Physically inadmissible condition is when there are no real solutions which satisfies $\beta_4 > 1$. In this case β_4 which are larger than 1 exist as conjugate complex numbers. When we plot α_4 versus the real values of four β_4 solutions, subcritical solution and supercritical solution merges at particular point of α_4 and shows only one real value, which indicates the real

value of conjugate complex numbers.

Evaluating downstream wake effect gives the solution for change in water elevation, but this will not be discussed in this research since we are not interested in the flow field but the extractable power.

2.3.4 Limitations of LMADT

Approximations used in LMADT should be discussed in order to apply the theory properly recognizing the limitations. One pivotal assumption is steady upstream flow, which seems contrasting to the unsteady tidal flow. However, considering the period of tidal cycle is around 25 hours, tidal flow can be assumed to be steady if the time scale of LMADT is small enough. LMADT itself does not provide any indication of the length scale, but experiment with porous disc conducted by Myers and Bahaj shows that velocity deficit of turbine flow recovers at around 20 turbine diameter downstream in a low blockage case [22]. The order of magnitude will be $O(10^2)m$, thus time required for steady solution of LMADT will be much shorter than the variation of upstream velocity for typical tidal flow.

Also, one-dimensional nature of the theory makes it hard to account for non-uniform upstream, drag forces, and bathymetry change along cross-streamwise direction when it is expanded to two-dimensional. However, variation along the tidal fence would have negligible effect on theoretical result of one tidal turbine if the fence is long enough than inter-turbine spacing. Therefore, LMADT is applicable for modeling tidal turbines.

Note again that LMADT cannot reflect the operation mechanism of the turbine device but just implies the idealized available tidal energy resource base on the second law of thermodynamics. In reality, less thrust will be exerted on the flow with non-normal direction due to vorticity in the wake. Nevertheless, yet simplified, LMADT provides concept of effect of tidal turbine on the flow and can be utilized for modeling energy extraction of tidal turbine and change in flow field in large scale.

2.2 Shallow Water Equation (SWE)

Two dimensional shallow water equation (henceforth SWE) is depth-integrated equation of three-dimensional Reynolds Averaged Navier-Stokes (RANS) equation, assuming vertical movement of water particle is negligible and pressure is hydrostatic. Two dimensional SWE can be written as a system of conservative PDE

$$\frac{\partial U}{\partial t} + \frac{\partial F}{\partial x} + \frac{\partial G}{\partial y} = S \quad (2.37)$$

where t is time, x and y are Cartesian coordinate, and U, F, G, S are column vectors which represents conservatives, x and y directional flux and source term, respectively. Including Coriolis force and bottom friction, these vectors are represented as Equation (2.38)

$$U = \begin{Bmatrix} \eta \\ uh \\ vh \end{Bmatrix}, \quad F = \begin{Bmatrix} hu \\ hu^2 \\ huv \end{Bmatrix}, \quad G = \begin{Bmatrix} hv \\ huv \\ hv^2 \end{Bmatrix}, \quad S = \begin{Bmatrix} 0 \\ -fvh - gh \frac{\partial \eta}{\partial x} + \frac{\tau_{b,x}}{\rho} \\ -fuh - gh \frac{\partial \eta}{\partial y} + \frac{\tau_{b,y}}{\rho} \end{Bmatrix} \quad (2.38)$$

where h is water depth, u and v are x and y directional depth-averaged velocity, respectively, τ_b is bottom friction, g is gravitational acceleration, η is free surface displacement which is $\eta = h - h_s$ where h_s is still water depth.

However, this SWE is nonlinear hyperbolic equation and has a risk of arise of discontinuity even if initial condition is smooth. Riemann solver is typically used to solve this shock problem. However, one can simplify this problem by artificially adding viscosity and include dispersion term $\nu \nabla^2 u$ inside the momentum balance equation. In this case reshaping the equation into non-conservative form is easier to handle. Changing the momentum balance equation, we get

$$\frac{\partial \mathbf{u}}{\partial t} + \mathbf{u} \cdot \nabla \mathbf{u} - \nu \nabla^2 \mathbf{u} + g \nabla \eta + \frac{\boldsymbol{\tau}_b}{\rho h} + \mathbf{T} = 0 \quad (2.39)$$

where $\mathbf{u} = (u, v)$, $\boldsymbol{\tau}_b = (\tau_{b,x}, \tau_{b,y})$ which can be modeled as proportional to velocity squared:

$$\tau_{b,x} = \rho C_f u \|\mathbf{u}\|, \quad \tau_{b,y} = \rho C_f v \|\mathbf{u}\| \quad (2.40)$$

and \mathbf{T} denotes sink term representing the tidal turbine. Continuity equation is

$$\frac{\partial \eta}{\partial t} + \nabla(h\mathbf{u}) = 0 \quad (2.41)$$

2.3 PDE-constrained Gradient-based Optimization using Adjoint method

Optimization scheme in OpenTidalFarm is gradient-based optimization and it is coupled with solving the governing equation of flow (Partial Differential Equation). The core algorithm for gradient-based optimization is computing the functional gradient $\frac{DJ}{Dm}$, where J denotes the target functional m denotes the controls. OpenTidalFarm uses dolfin-adjoint module to compute functional gradient efficiently, with consistent speed for computation even for large tidal farm containing over hundreds of turbines. It is based on adjoint method thus the PDE should be rederived for into a linear equation for adjoint variable. After computing the functional gradient, the control is updated toward the direction of derived functional gradient, but the magnitude depends on the optimization algorithm. Sequential Quadratic Programming (SQP) is known to show good performance for constrained optimization.

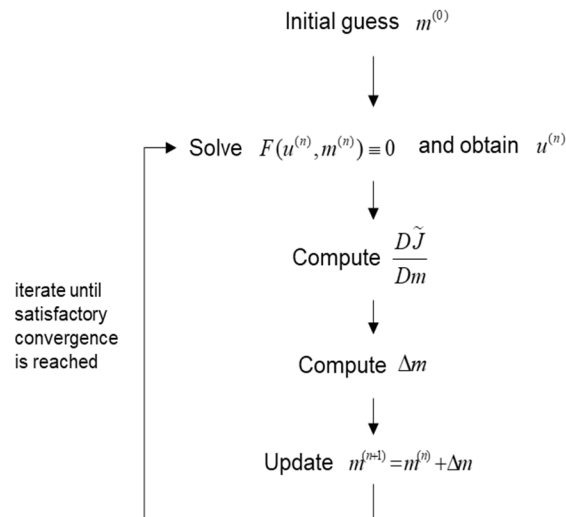


Figure 8 Flow chart of gradient-based optimization.

2.3.1 Gradient-based Optimization

In general, PDE-constrained optimization problem can be generalized as:

$$\begin{aligned}
 & \min_{u,m} J(u, m) \\
 & \text{subject to} \\
 & F(u, m) = 0 \\
 & l_u \leq m \leq l_b \\
 & g(m) = 0
 \end{aligned} \tag{2.42}$$

where $u \in \mathbb{R}^U$, $m \in \mathbb{R}^M$, $J: \mathbb{R}^{U \times M} \rightarrow \mathbb{R}$, $F: \mathbb{R}^{U \times M} \rightarrow \mathbb{R}$. For maximization problem, it can be treated as minimization problem by reversing the sign of functional of interest. $F(u, m) \equiv 0$ is vector expression representing a system of PDE that describe the physics of the given problem. It is also called state equation. Note that the functional of interest is functional of an implicit function $u(m)$. We never have an explicit expression for u in terms of m . But still, we can discuss (or compute) its derivative, du/dm and use it for computing dJ/dm .

In most case, we assume that the PDE yields a unique solution u for every m because the state equation is well-posed for u in which m appears as parameter [15]. This allows to define an operator $u(m)$ which is unique corresponding solution for every $m \in \mathbb{R}^M$. We can convert constrained problem into unconstrained problem by substituting PDE solution operator $u(m)$. This form of optimization problem is called reduced problem:

$$\begin{aligned}
& \min_m J(u(m), m) \\
& \text{subject to} \\
& l_u \leq m \leq l_b \\
& g(m) = 0
\end{aligned} \tag{2.43}$$

We define the substituted, pure functional of m as reduced functional, that is:

$$\tilde{J}(m) := J(u(m), m)$$

To compute $\tilde{J}(m)$, one must first solve the state equation and find state variable, and then evaluate $J(u, m)$. Both (2.42) and (2.43) have advantages and disadvantages. Nevertheless, there are strong advantages for using reduced formulation. One of the advantages of using reduced functional is that the PDE constraint is exactly satisfied at each optimization iteration by implicitly solved for in the reduced function, while non-reduced formulation is generally based on optimization algorithms which treats PDE constraint linearly [10]. Also, non-reduced formulation should optimize both the state variable u and the controls m , indicating that the number of free variables can exponentially increase in cases when the problem is transient, has a large computational domain, or contains complex bathymetry which makes high resolution mesh is necessary. The optimization problem which the module targets is coupled with Shallow Water Equations applied in tidal strait modeling. Thus, the characteristics of the problem—nonlinearity of the Shallow Water Equation (SWE), unsteadiness of tidal current, and the scale and complexity of tidal farm site—provide suitable reason for selecting reduced formulation for the model. Since the PDE-constraint is built-in to the reduced functional, we can reduce PDE-constraint and convert the problem into a simpler, unconstrained one.

Chapter 3. Methodology

3.1 Specifications of OpenTidalFarm

In this research, *OpenTidalFarm* is selected as optimization tool of large number of tidal array, which is a python-based open source code developed by Funke et. al [4]. *OpenTidalFarm* uses gradient-based PDE-constrained optimization technique applying adjoint method to find functional gradient efficiently for a large number of parameters. For each iteration step, it solves two-dimensional finite element nonlinear shallow water equation. Turbine is modeled as additional bed friction term at the location of turbines. Array configuration is updated with SLSQP algorithm included in SciPy optimization package. Unstructured triangular grid is generated using Gmsh. Software and code are available at <http://OpenTidalFarm.org>.

3.1.1 Design Parameters

In this optimization problem of array configuration, we aim for find the optimal positions of individual turbines in two-dimensional plane. Assuming that turbines are individually tuned, the design parameter m is set as

$$m = \{K_1 K_2 K_3 \cdots K_N x_1 y_1 x_2 y_2 x_3 y_3 \cdots x_N y_N\} \quad (4.1)$$

where K_i denotes friction coefficient of i^{th} turbine and (x_i, y_i) is location of i^{th} turbine.

3.1.2 PDE constraint

Target functional is function of two dimensional velocities, u and v , which are obtained by solving SWE. Format of equation is described in length at section 2.2. Adding the turbine thrust,

$$\frac{\partial \mathbf{u}}{\partial t} + \mathbf{u} \cdot \nabla \mathbf{u} - \nu \nabla^2 \mathbf{u} + g \nabla \eta + \frac{C_f + C_T}{h} \mathbf{u} \|\mathbf{u}\| = 0 \quad (4.2)$$

Therefore, SWE with additional bed friction is the PDE constraint of optimization problem. PDE is represented as $F(z, m) = 0$ where $F(z, m)$ is PDE operator representing SWE and $z = (u, \eta)$ is solution of PDE.

3.1.3 Turbine Parameterisation

In shallow water equation based modeling, turbine has been implemented as adding extra bed friction proportional to momentum flux from various prior researches [11, 32, 33]. Drag associated with existence of turbine is added along the tidal fence and zero elsewhere. However, constant parameterisation is problematic in gradient-based optimization because friction becomes non-differentiable. Therefore, friction is increased smoothly as bell-shaped bump function within turbine radius.

$$\phi_{p,r}(x) = \begin{cases} \exp(1 - 1 / (1 - \|\frac{x-p}{r}\|)) & \text{for } \|\frac{x-p}{r}\| < 1 \\ 0 & \text{otherwise} \end{cases} \quad (4.3)$$

where x is x coordinate and p is location of turbine center. Since the simulation domain is two-dimensional, we need to smooth the turbine friction in both x and y directions. The

friction function for i^{th} turbine is expressed as

$$C_i(m)(x, y) = K_i \phi_{x_i, r}(x) \phi_{y_i, r}(y). \quad (4.4)$$

Turbine properties can be modified by calibrating K_i . Default option for K_i is uniform constant for all turbines. Sum of the turbine friction functions for N turbines becomes

$$C_T(m) = \sum_{i=1}^N C_i(m). \quad (4.5)$$

Smoothed turbine friction function with $K=1$, $x=10$, $y=10$ and $r=5$ is plotted in figure 10.

3.1.4 Target functional

Target functional is the value of interest that is to be maximized, which is time averaged power extracted from the array of turbines. Time average is required due to the non-stationary of governing equation. Tidal current has periodicity in its speed and height, thus target functional should include the varying power output over varying flow field over time.

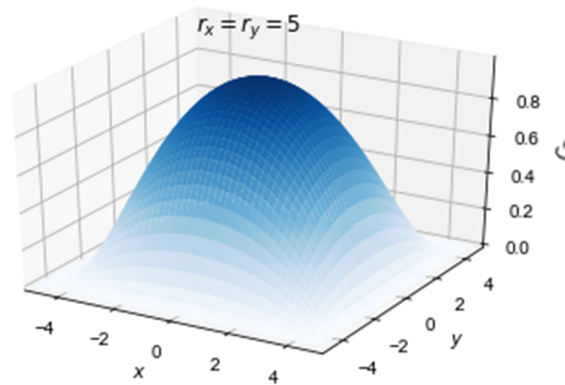


Figure 9 Smoothed friction function with $K=1$, $x=10$, $y=10$ and $r=5$.

$$J(u, m) = \frac{1}{T} \int_0^T \int_{\Omega} \rho C_T(m) \|\mathbf{u}\|^3 dxdt \quad (4.6)$$

In addition to the target functional, thrust exerted on the water body over the turbine representation area is

$$T(u, m) = \frac{1}{T} \int_0^T \int_{\Omega} \rho C_T(m) \|\mathbf{u}\|^2 dxdt \quad (4.7).$$

More advanced functional can be presented by incorporating costs of tidal farm installation, such as cable inter-connecting or potential environmental effect. Recently, OpenTidalFarm is updated with integrating location based costs and profit-maximisation functional [6].

3.1.5 Box and inequality constraints

The box and inequality constraints are used to confine the available values for optimization parameters. In the context of wind farm, wind direction is random variable assumed to following wind direction PDF. This characteristic of wind makes downstream and lateral spacing important to minimize turbine interaction due to wake effect. It is rule of thumb to have minimum downstream and lateral spacing of $10D$ and $5D$, respectively.

For the tidal turbine configuration problem, in contrast, direction of tidal current does not change significantly, except that the magnitude of velocity vector varies from u to $-u$. Therefore, due to the small uncertainty in current direction, lateral spacing between turbine might be not important as it is in wind farm design. Nevertheless, minimum lateral spacing would be reasonable to apply in context of construction of device structure. For downstream spacing, Lee et al. [21] simulated turbine in three-dimensional model for small

number of tidal turbine arrays and showed that turbine efficiency drops when downstream spacing is less than $3D$. Note that simulation examples in Funke et al. used constraint with inter-turbine spacing is less than $3D$ [10]. This constraint will yield less optimized power compare to the unconstrained optimization. Even if a row of array is facing the current in normal direction, individual turbines within the row should have lateral spacing of $3D$ due to the constraint which might be too much. However, since the configuration of array is not optimized in structured form, it is difficult to define the direction of lateral within two turbines. Therefore, constraints will be used analogous to one of described in Funke et al. [10], which is

$$\| p_i - p_j \|^2 \geq d_{\min}^2, \text{ for } 1 \leq i < j \leq N. \quad (4.8)$$

Box and inequality constraints in Equation (4.8) are concave function thus satisfies the Concave Constraint Qualification (CCQ). CCQ is required to determine whether the optimization problem is well-posed.

3.1.6 Gradient-based optimization with adjoint approach

Gradient-based optimization algorithm updates the optimization parameter using information of derivatives of the target functional with respect to the parameters. In OpenTidalFarm, sequential quadratic programming (SQP) is used for updating parameters for each iteration.

Calculation of functional gradient with respect to set of parameters m requires high computational cost as number of turbines increases. Efficient computation of functional

derivative is achieved by adjoint method. Functional gradient is obtained as

$$\begin{aligned}\frac{dJ}{dm} &= \frac{\partial J}{\partial F} \frac{\partial F}{\partial m} + \frac{\partial J}{\partial m} \\ &= \lambda \frac{\partial F}{\partial m} + \frac{\partial J}{\partial m}\end{aligned}\tag{4.9}$$

where adjoint solution λ is obtained by solving adjoint equation

$$\lambda \frac{\partial F}{\partial z} = \frac{\partial J}{\partial z}.\tag{4.10}$$

Rather than deriving and discretizing the adjoint equation, OpenTidalFarm used finite element discretization high-level algorithmic differentiation approach called FEniCS. This efficiently and automatically derives and implements the discrete adjoint model. Unstructured mesh is generated with Gmsh to conform complex basin geometries.

3.2 Realistic Actuator Disc Modeling in 2D SWE

Before elaborating on specific modeling for optimization, pilot test was undertaken using the example settings suggested in Funke et. al. [10]. The purpose of pilot test is to get insight for advanced modeling and to figure out difference between LMADT and turbine modeling in OpenTidalFarm. A single tidal device with diameter of 20m was deployed and SWE was solved.

It should be recalled from chapter 2 that LMADT is based on quasi-inviscid flow assumption. This assumption was crucial because it enables to model the turbine flow and bypass flow separately and later mixed in far downstream. However, the assumption is

only valid for cases when the applied thrust is small; when the strong thrust is applied, spanwise velocity gradient will be large and two flows will be mixed together because of strong momentum diffusion.

3.2.1 Actuator disc modeling in 2D SWE and 3D flow model

Actuator disc modeling assumes tidal device as a thin penetrable disc where disc is in circular shape with identical size of turbine device's frontal area. Therefore, for accurate flow modeling with actuator disc, 3D flow modeling should be appropriate because it can reveal vertical anomaly of wake flow. However, using 3D governing equation for the flow would be too much expensive for PDE-constrained optimization problem. This makes 2D SWE modeling inevitable for this study, and thus actuator disc should be implemented in 2D SWE equation.

The main difference between 2D SWE model and 3D flow model is that SWE

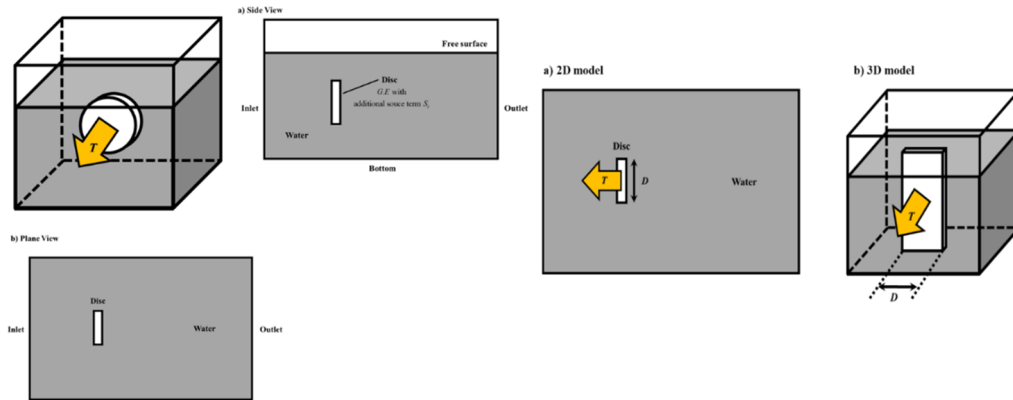


Figure 10 (Left) Schematic drawing of 3D actuator disc modeling. a) Plane view is identical to 2D actuator disc modeling, b) disc area is partially spanning the water depth. (Right) Schematic drawing of 2D actuator disc modeling in SWE. a) Plane view is identical to 2D actuator disc modeling, b) disc area is fully spanning the water depth.

ignores vertical flow profile and assume vertically uniform flow. 3D actuator disc modeling is applied by adding the thrust as sink term only for the turbine represented zone. In similar sense, 2D actuator disc modeling can be applied as a thrust divided by water depth. It should be noted that this kind of sink term application indicates that thrust is applied for the whole vertical water column in 2D actuator disc modeling. Therefore, array frontal area A_D should be defined as DH_0 , which is the rectangular area described in figure 11. C_p should be calculated with this modified A_D .

3.2.2 Wake properties behind tidal turbine

Optimized array shape will largely dependent on the velocity deficit along the downstream wake. If wake velocity recovers fast, optimized array can be aligned compactly in downstream direction. Otherwise if wake velocity recovers slowly, large spacing along downstream direction will be required. Therefore, modeled turbine should yield wake with similar properties observed in unsteady 3D modeling.

According to various previous researches on wake structure behind an isolated turbine, velocity at near wake zone ($x < 3D$, where x is downstream distance from disc centre) is largely dependent on turbine spec. However, in general, velocity at the $x=5D$ and $x=10D$ downstream lied within range of 65-75% and 70%-80% of upstream velocity, respectively. Additionally, flow recovers 90% of its upstream velocity at $x=20D$ downstream.

Table 1 Summarized list of studies on wake properties behind the tidal device.

	Researcher	Turbine type	Flow modeling
<i>Experiment</i>	Stallare T. et. al (2013)	Three-blade turbine	
	Myers and Bahaj (2010)	Perforated disc	
<i>Numerical simulation</i>	Sun et. al (2007)	Perforated disc	VOF RANS
	Turnock. et. al (2011)	BEMT	RANS
	Churchfield et. al (2013)	Actuator line	LES
	Harrison et. al (2010)	Perforated disc	VOF RANS

BEMT: Blade Element Momentum Theory, VOF: Volume of Fraction
RANS: Reynold's Averaged Navier-Stokes Eq., LES: Large-Eddy Simulation

3.2.3 Simulation settings for tuning K and ν

Specifications of simulation settings will be discussed. Mesh and boundary conditions were designed to reflect tidal flow modeling. To generate similar velocity, deficiency for steady state solution of actuator disc implemented 2D SWE, turbine thrust coefficient K and artificial viscosity ν are varied.

3.2.3.1 Mesh domain

Rectangular domain was generated using Gmsh v2.0. Simplified tidal channel is 900 m×600 m in size, while the farm site is 300 m×500 m in size apart from the lower-left corner. To ensure tidal turbine is properly resolved regardless of turbine position during

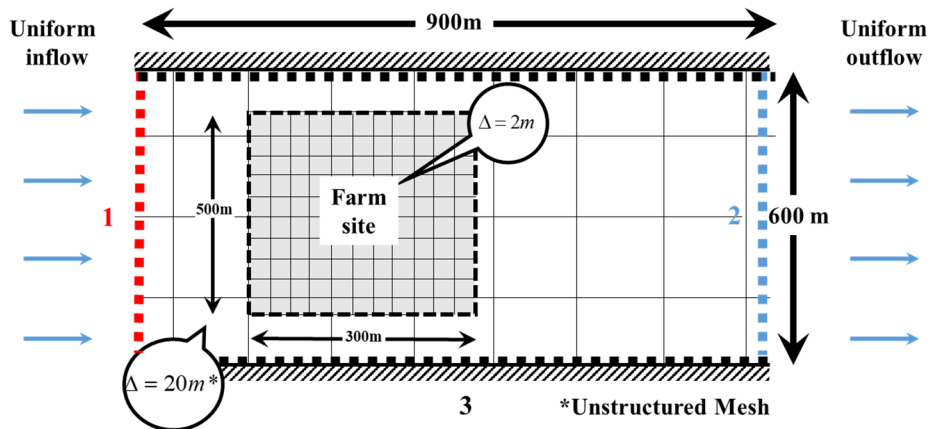


Figure 11 Schematic representation of simulation domain for single turbine tuning , pilot test 2 and main test.

array optimization, farm site is meshed in 1 m, alternated structured grid. Alternated grid is preferable to one-sided (left or right aligned) grid in order to eschew accumulation of numerical error. Outside the farm site is meshed by using unstructured mesh, where the grid size at the boundary is 20m. Number of total grids are around 46569. The generated .msh file should be converted to .xml type file for compatibility with DOLFIN (FeniCS's C++ backend), and once more converted to new version of xml to ensure compatibility with MPI.

3.2.3.2 Boundary conditions

Boundaries of rectangular domain are classified into three types; inlet, outlet and the walls. Affiliated nodes for the boundaries are labeled as integer 1, 2 and 3, respectively.

Table 2 Summary of mesh used in single turbine modeling, pilot test 2 and main test.

Site	outside	Grid size	#. Grid
Farm site	Structured (alternated)	$\Delta x = 2m$ (isosceles tri.)	46569
Elsewhere	Unstructured	$\Delta x_{\max} = 20m$ (isosceles tri.)	

Since the LMADT is based on steady and uniform flow, boundary conditions were applied in an analogous sense. In the simulation, inlet flow velocity was intended to be 2m/s along the channel cross-section.

However, clamping the inlet as the designated velocity is improper considering the hydrodynamic change induced by tidal farm. When the tidal devices are implemented in subcritical tidal current, energy loss in the flow induces water level drop at the downstream. This hydrodynamics is reflected in free-surface LMADT. Thus, analyzing extracted power from optimized array with LMADT is only valid when the flow just passes through the outlet without influencing inner domain. Although not mentioned in LMADT (because it assumes steady inlet flow), existence of tidal device changes the flow near the turbine and the changed property of the flow propagates to both downstream and upstream. Clamping the boundary condition would be obviously contradictory to physics in natural tidal current. Thus, proper open boundary condition should be provided at the end outlet to ensure the flow leave the domain with minimal effect on the upstream flow.

Open boundary conditions are necessary for regional tidal modeling containing

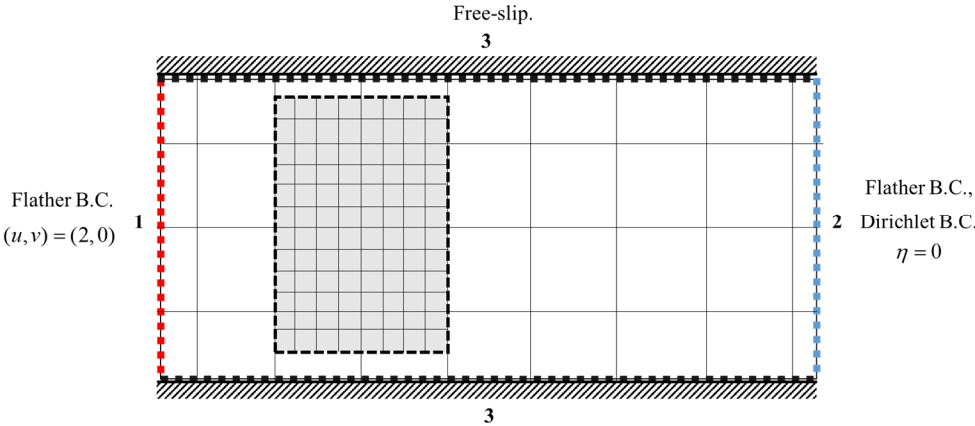


Figure 12 Schematic representation of simulation domain for optimization.

non-land boundaries [4]. In this study, we select Flather boundary condition among various open boundary conditions because it is the only option for open boundary condition in OpenTidalFarm. Flather condition is extension of a radiation boundary condition, which are based on the propagation of a conservative quantity ϕ on the boundary Γ [9].

$$\frac{\partial \phi}{\partial t} + c \frac{\partial \phi}{\partial n} = 0 \quad (4.11)$$

where c is celerity of quantity propagating through the boundary and n is normal direction at the boundary. For a case of long wave, wave celerity is approximated as \sqrt{gH} where g is gravitational acceleration and H is water depth. Approximating continuity equation for depth-averaged shallow water equation is

$$\frac{\partial \eta}{\partial t} + H \frac{\partial U_n}{\partial n} = 0 \quad (4.12)$$

where η is water elevation from the still water level and U_n is depth-averaged n -directional velocity. Coupling (4.11) and (4.12) for setting $\phi = \eta$ gives

$$\frac{\partial}{\partial n} \left[U_n - \sqrt{\frac{g}{H}} \eta \right] = 0 \quad (4.13)$$

which yields

$$u - u_* = \sqrt{\frac{g}{H}} (\eta - \eta_*) \text{ on } \Gamma \quad (4.14)$$

where u_* and η_* are expected velocity and free surface elevation at the boundary grids.

The final form indicates that the difference between the expected and simulated free

surface is allowed to propagate out of the domain.

In finite element method (FEM), Flather boundary condition is applied into weak form of the governing PDE, i.e. steady SWE. Formulated FEM equations are

$$\int_{\Omega} (u \cdot \nabla u) \psi d\Omega + \int_{\Omega} \nu \nabla u \cdot \nabla \psi d\Omega + \int_{\Omega} g \nabla \eta \psi d\Omega + \int_{\Omega} \frac{c_b + c_T}{H} u \|u\| \psi d\Omega = 0 \quad (4.15)$$

$$-\int_{\partial\Omega} (Hu) \cdot \nabla \phi d\Omega + \int_{\partial\Omega} (Hu \cdot n) \phi dS = 0 \quad (4.16)$$

where ψ and ϕ are test functions (or approximate functions) of u vector and h , respectively. Note that the degree of elementwise test functions are all 2. The upper and lower equation correspond to the weak form of momentum equation and continuity equation, respectively. It is applied at surface integral term in continuity equation (i.e., in a weak sense). From this property, even though we specify the inlet velocity expression for Flather boundary conditions, inlet velocity is not exactly matched as prescribed.

Flather boundary was specified for inlet and outlet flow with $u_* = 2m/s$. Wall boundaries are applied with free-slip boundary conditions with no normal flow, i.e. $\underline{u} \cdot \underline{n} = 0$. Since the Flather boundary condition is applied in a weak sense just for u , we additionally need to specify one more Dirichlet condition for η in order to determine FEM solution. Thus, a clamped boundary condition, $\eta = 0$ was applied at the outlet (boundary 2). This was inevitable because applying identical boundary condition for the inlet (boundary 1) returned zero-valued velocity field.

3.2.3.3 Parameter settings

The simulation domain is idealization of actual tidal strait, and parameters used in the simulation was aimed to model realistic tidal current as much as possible. In most cases, Froude number at potential tidal stream farm candidates ranges from 0.1 to 0.2. Setting the design Froude number as 0.1, water depth of the channel should be around 50m for the given inlet velocity of 2m/s. Note that both the water depth and inlet velocity is plausible for natural tidal currents [7, 28]. According to Stallard et. al, typical commercial tidal turbine device is designed to be implemented in water with depth ranges with 1.5-3.0 times turbine diameter D [28]. Therefore, D as 20m was set as appropriate size of turbine in a simulation in this problem.

Bottom friction coefficient was adopted from Funke et. al., where the value is 0.0025 [10]. SWE does not contain turbulence model explicitly, but using a large viscosity coefficient can be regarded as eddy viscosity model is included and thus eddy viscosity coefficient ν_T is added besides the kinetic viscosity ν_k in the divergence term. Note that the flow should be Newtonian flow in order to use eddy viscosity model. In short, viscosity coefficient ν in the governing equation (4.2) is sum of ν_t and ν_k , and it would be natural to regard $\nu \approx \nu_T$ because the order of magnitude is significantly different (i.e. $\nu_T \gg \nu_k$). Funke et. al used $\nu = 3m^2 / s$, but in this study we will find out realistic value for ν in order to resolve realistic wake.

Base on the fact that typical tidal stream device is in order of $o(10m)$ and considering the practicality (i.e., to deploy more than 10 tidal devices along the channel cross-section).

Table 3 Parameter settings for pilot test

Parameter	Value
Water depth, H	50m
Viscosity coefficient, ν	varied
Gravitational acceleration, g	9.81 m/s ²
Water density, ρ	1025 kg/m ³
Bottom friction coefficient, c_b	0.0025
Turbine diameter, D	20m

3.2.4 Simulation results

Velocities along the centerline behind the turbine was normalized by upstream velocity and plotted versus normalized distance from the device. Matching with the discussion in section 3.2.2, case with $K=10$ and $\nu = 2\text{m}^2/\text{s}$ was selected as suitable coefficient set. For this case, an isolated turbine has power of 2.75MW and its C_p is 0.6721. This value is compared with a commercial turbine with similar D , MCT's SeaGen S model. SeaGen S turbine has a diameter of 20m and its rated power for rated speed

Table 4 Several specifications of commercial tidal turbines, adopted from Roberts et. al [26]

Developer	Atlantis	Bourne	MCT	Verdant	Voith
Device	AR1000	RiverStar	SeaGen S	Gen5	1 MW test
Rated power (W)	1.00×10^6	5.00×10^4	2.00×10^6	1.68×10^3	1×10^6
Rated flow speed (m/s)	2.65	2.05	2.40	2.59	2.90
No. of rotors (-)	1	1	2	3	1
Rotor diameter (m)	18.0	6.09	20.0	5.00	16.0
Rotor swept area (m ²)	254	29	314	20	201
Rated C_p	0.41	0.39	0.45	0.35	0.40

2.4m/s is 2MW, where rated C_p is 0.45. It seems that modeled turbine overestimates available power, but still gives reasonable values and wake properties and thus plausible to be selected. Except for the pilot test 1, K and ν will be used as this value.

Also, it would be notable to stress that the simulated flow reveals the hydrodynamics derived from LMADT. Slowest velocity is detected at the near-wake zone with is within $2D$ in downstream direction, and pressure field shows that spanwise pressure equilibrium is reached at the near-wake zone. This indicates that quasi-inviscid flow assumption in LMADT is acceptable. Again note that quasi-inviscid assumption is the

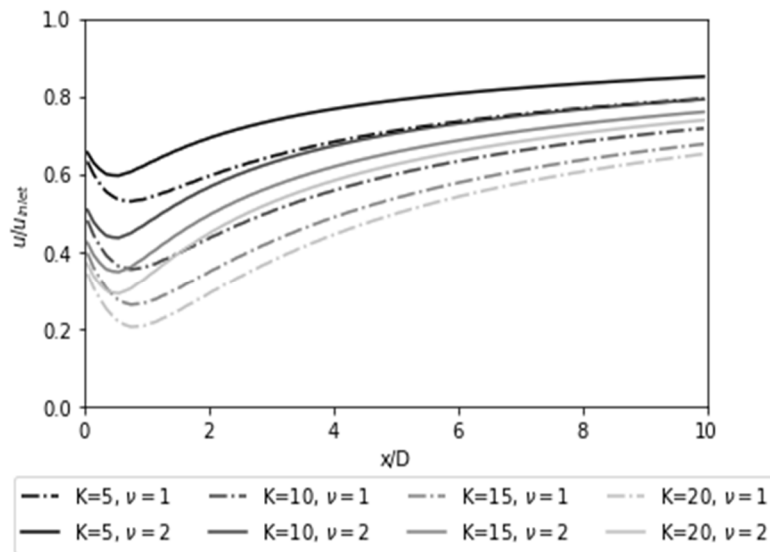


Figure 14 Normalized velocity along downstream wake by upstream velocity, U_{init} .

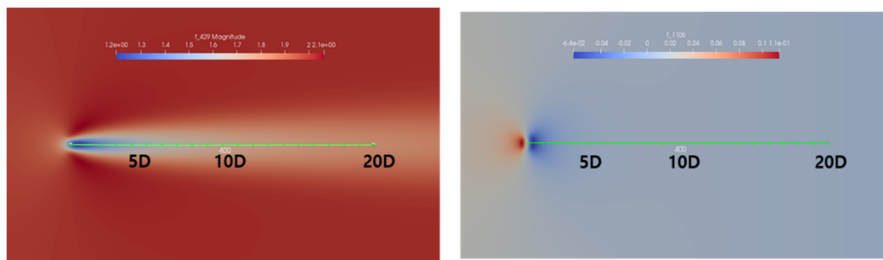


Figure 13 (Left) velocity field and (Right) pressure field with selected K and ν .

pivotal assumption for LMADT which enables separated modeling of turbine flow and bypass flow.

3.3 Pilot Test 1: effect of initial condition and number of turbines on optimization result

To get valuable insight for the general pattern or trend of optimal array configuration, coordinates of tidal devices were optimized for various number of turbines implemented idealized rectangular tidal channel domain. Width of the channel domain is fixed and total number of turbines vary from range of eight to fifteen. Also, various initial conditions were given and the following optimization results were compared to overcome the limitation of gradient-based optimization and find the near-global maximum results.

3.3.1 Simulation settings

Pilot test 1 was undertaken with simulation settings described in Funke et. al [10], which is the development document of OpenTidalFarm. This test was conducted at the very beginning at the research so it simply adopted simulation settings described at the aforementioned paper. Note that boundary condition, K and ν are different to other simulations which makes difference in isolated turbine power. Individual power in pilot test 1 is 3.3MW with C_p of 0.8049.

3.3.1.1 Mesh domain

Rectangular domain was generated using Gmsh v2.0. Simplified tidal channel is 640 m×320 m in size, while the farm site is one fourth of entire domain size. To ensure

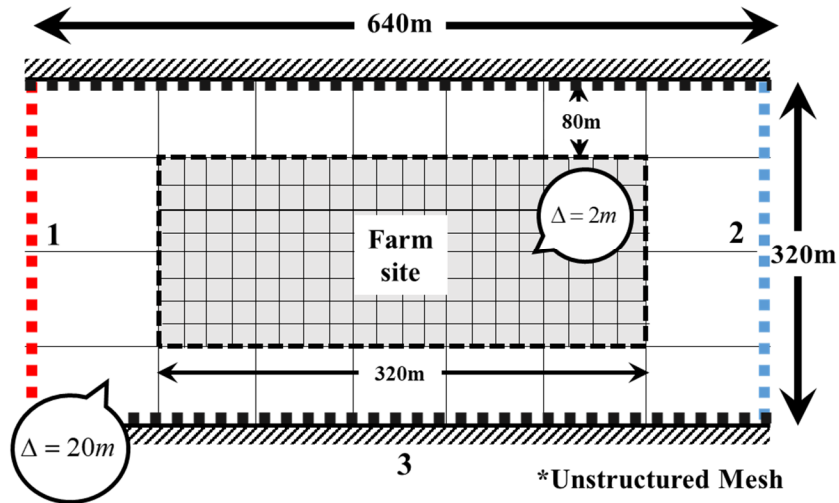


Figure 15 Schematic representation of simulation domain for pilot test 1

tidal turbine is properly resolved regardless of turbine position during array optimization, farm site is meshed in 2 m, alternated structured grid. Alternated grid is preferable to one-sided (left or right aligned) grid in order to eschew accumulation of numerical error. Outside the farm site is meshed by using unstructured mesh, where the grid size at the boundary is 20 m. Number of total grids are around 33000.

3.3.1.2 Boundary conditions

Three boundaries are specified during mesh generation step; 1 for left side inlet, 2 for right side outlet, and 3 for remaining boundaries. In the pilot test, response of inlet and outlet flow due to the existence of turbine was ignored and simple boundary conditions such as Dirichlet and free-slip boundary conditions were applied. Boundary condition for

Table 5 Summary of simulation domain for pilot test 1.

Site	outside	Grid size	#. Grid
Farm site	Structured (alternated)	$\Delta x = 2m$ (isosceles tri.)	32795
Elsewhere	Unstructured	$\Delta x_{max} = 20m$ (isosceles tri.)	

the inlet (boundary 1) was given as Dirichlet boundary condition with $(u, v) = (2, 0)$ m/s. Since each variable u, v and η should be specified at least for one boundary, boundary condition for the outlet was assigned as $\eta = 0$. Free-slip condition (i.e. no normal flow, $\underline{u} \cdot \underline{n} = 0$) was applied elsewhere (boundary 3).

3.3.1.3 Parameter settings

Parameter settings are identical to the one used in the pilot test. In addition, minimum turbine distance (d_{\min}) was set as 15m which is 1.5 times of the device diameter. This condition is provided as inequality constraint for array position optimization. Following the mother paper, $v = 2\text{m}^2/\text{s}$ and K was set as 21.

3.3.1.4 Test cases

Pilot test 1 aims to observe the effect of initial condition by changing number of turbines. Thus, size of farm site was fixed as $L_x = 320\text{m}$, $L_y = 160\text{m}$ and also d_{\min} was fixed as $1.5D$ (i.e. 30m). Number of turbine was varied from 3 to 8. Initial conditions are by default regular and Latin Hypercube Sampling (LHS) method, and if it is needed case-dependently modified initial conditions are also tested for some cases. Latin Hypercube Sampling (LHS) method was used to set initial turbine array configuration randomly. LHS is feature with no overlapping in generated sample's x and y positions, comparing respectively. In case of positioning N turbines, LHS method divides x and y axis of the domain into N equal segments (domain is divided in N^2 grids), and then randomly take N x and N y values within each corresponding segments. Position of each turbine is generated by randomly pairing x and y coordinates. Since LHS gives randomly scattered coordinates, LHS was undertaken 10 times for each N and the optimized array results were

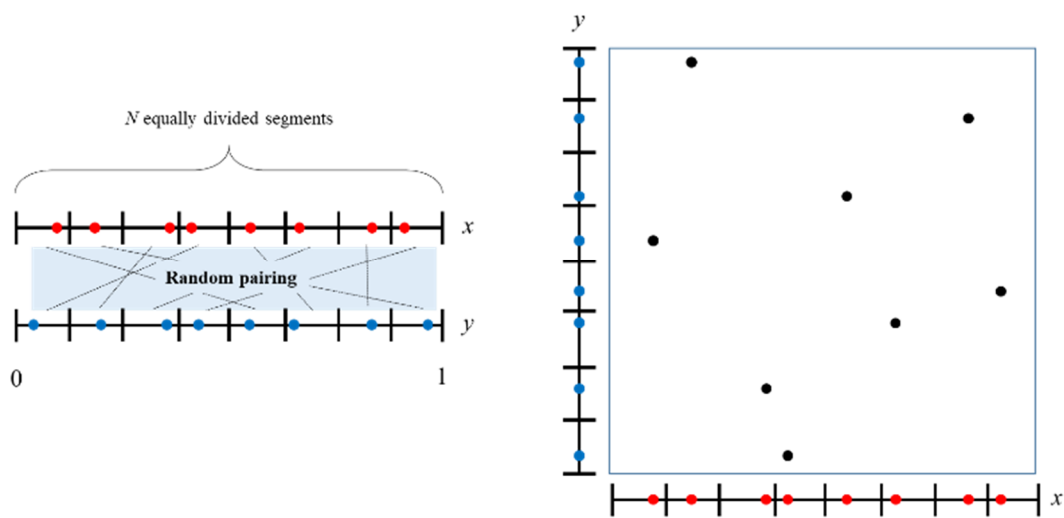


Figure 16 Concept description of LHS.

overlapped into one figure in order to see the trend of local optimal solution.

3.3.2 Simulation results

For brevity, figures and tables containing optimization result are listed in Appendix A. Pilot test 1 contains comparably few test cases and the results are easily noticeable by just observing the raw data. Thus, rather than discussing results here, intuitive conclusions induced from the results will be straightly stated in the next section.

3.3.3 Conclusions of pilot test 1

Three pre-conclusions for pilot test 1 are the following. First, optimization result is highly dependent to initial condition. This conclusion was predictable since the optimization problem is very complex, coupled with nonlinear PDE. Second, when it is available, deploying turbines as uniformly spaced linear barrage shape gives good

performance. This type of array configuration is available when $\frac{Nd_{\min}}{L_y} > 1$. Third, when linear barrage is impossible because $\frac{Nd_{\min}}{L_y} > 1$, uniformly spaced curved barrage shape gives good result. Finally, it was observed that V-shape initial condition converges to decent optimal array configuration which is an all-connected array with curvature resembling arc.

Extending this valuable results, another pilot test was designed and named as pilot test 2. Also, later it will be shown that the conclusion from pilot test 1 also coincides with the final conclusion of this study.

3.4 Pilot Test 2: effect of minimum distance constraint and spanwise length of the farm site on optimization result

In section 3.3, pilot test 1 was conducted by varying N and initial conditions. On the other hand, pilot test 2 aims to discover the impact of minimum distance constraint d_{\min} and spanwise length of the farm site L_y on the optimized configuration. Through pilot test 2, valuable insights could be obtained and used to design the main test in section 3.5.

3.4.1 Simulation settings

Simulation settings for pilot test 2 is different to pilot test 1. It is designed with more caution and attempted to reveal more physical solution. Simulation setting is almost

identical to section 3.2.3 and this is obvious because section 3.2 was designed to tuning simulation parameters which will be used for this pilot test 2 and further the main test. Therefore, only some difference between section 3.2.3 will be described for each sections.

3.4.1.1 Mesh domain

Mesh domain is identical to section 3.2.3.1 because unless the performance of isolated turbine in the pilot test 2 will be different to the one described in section 3.2. Therefore, farm site was fixed as an excessively long length (i.e. 500m) comparing with L_y which was provided as an optimization constraint during the optimization process.

3.4.1.2 Boundary conditions

Boundary conditions used in pilot test 2 is exactly identical to section 3.2.3.2. Therefore, there will be no need for further discussion on this part and it is rather recommended to look section 3.2.3.2 for detailed contents.

3.4.1.3 Parameter settings

Parameter settings used in pilot test 2 is exactly identical to section 3.2.3.3. Therefore, there will be no need for further discussion on this part and it is rather

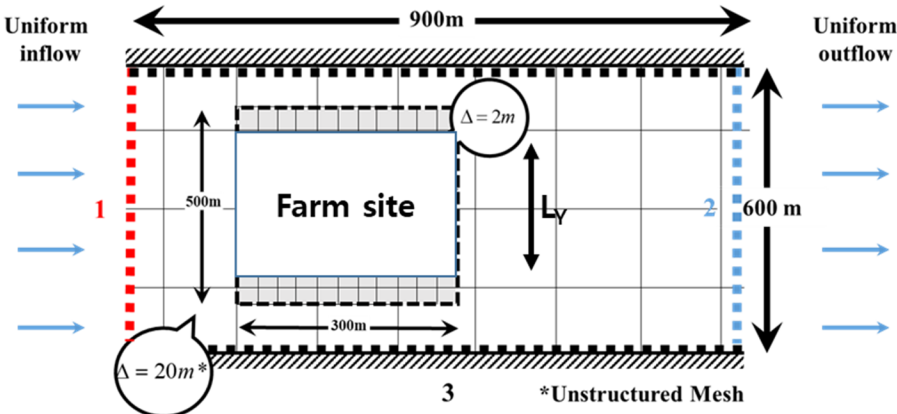


Figure 17 Mesh domain and farm constraint used in pilot test 2 and main test.

recommended to look section 3.2.3.3 for detailed contents.

3.4.1.4 Test cases

Pilot test 2 aims to observe the effect of d_{\min} and L_y . Thus, N was fixed as 8 and initial condition was fixed as V shape initial condition, which were customized for each case of d_{\min} and L_y . L_x was fixed as 320m and only L_y was varied as 5 values: (1) 370 m, (2) 345 m, (3) 320 m, (4) 295 m, (5) 270m. Also d_{\min} was varied as 4 values: (1) 1.5D, (2) 2.0D, (3) 2.5D, (4) 3.0D (i.e. 30m, 40m, 50m and 60m). In summary, 20 cases of optimization was conducted for pilot test 2 by varying d_{\min} and L_y .

Initial condition was selected as V shape, and this was motivated from the conclusion of pilot test 1. To recall, V shape initial condition showed high tendency of ending with optimal (or decent) configuration. V shape was initially given as symmetry shape with direction of \angle . Distance between adjacent turbine was forced to be d_{\min} because optimized result does not show significant change when initial condition was given as sparse configuration. This result lies on the fact that turbine by turbine interaction is reduced with sparse configuration and its symmetry makes initial condition as local optima (or saddle point). For this reason, initial condition was provided as compact as possible, while remaining its V shape.

3.4.2 Simulation results

For brevity, figures and tables containing optimization result are listed in Appendix B. In this section, mainly three manipulated results will be discussed in detail.

In total 20 cases were optimized and it is almost obvious that optimized results are local optima in general. Still, it was available to classify the optimized array configuration into some groups: coagulated linear barrage, uniform linear barrage, irregularly jiggered linear barrage, slightly modified from initial condition, and finally no change from initial condition. Normalized parameter, $\frac{Nd_{\min}}{L_Y}$ was calculated for each cases and relation between the classified optimized configuration was analyzed. Rough range of $\frac{Nd_{\min}}{L_Y}$ is suggested, however, it was unable to articulately discretize the range of $\frac{Nd_{\min}}{L_Y}$ corresponding to the classified array shape. Nevertheless, it is evident that $\frac{Nd_{\min}}{L_Y}$ is an influential variable for the optimized array configuration.

	1.5D	2.0D	2.5D	3.0D
370m	0.6486	0.8649	1.081	1.297
345m	0.6956	0.9275	1.159	1.391
320m	0.7500	1.090	1.250	1.500
295m	0.8135	1.085	1.356	1.627
270m	0.8889	1.185	1.482	1.778

Coagulated linear barrage	Uniform linear barrage	Jagged linear barrage	Slight change from initial condition	No change from initial condition
$\frac{Nd_{\min}}{L_Y} < 0.9$	$0.9 < \frac{Nd_{\min}}{L_Y} < 1.15$		$1.05 < \frac{Nd_{\min}}{L_Y} < 1.4$	$\frac{Nd_{\min}}{L_Y} > 1.3$

Figure 18 Value of (Nd_{\min}/L_Y) for 20 subcases in pilot test 2. Specific color indicates the type of optimized array configuration.

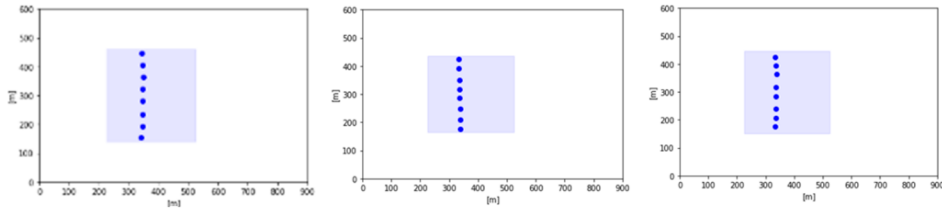


Figure 19 Optimized results with highest performance. (left) $d_{\min}=2D$ and L3, (center) $d_{\min}=1.5D$ and L5, (right) $d_{\min}=1.5D$ and L4.

Among the 20 cases, highest power outputs were obtained from (nearly) uniformly spaced linear barrage types, with a small curvature. These nearly optimal array configuration yields 28.6% increase in power performance comparing with multiplying N to P_i (i.e. power from 8 isolated turbines). This is remarkable result because turbine array does not perform better than isolated turbines in many cases. For example, regular array in rectangular shape (4 rows 2 column) rather perform inferior than isolated turbines. Performance of uniformly spaced turbine was tested by varying d_{\min} from 1.4D to 2.5D. Optimal $d_{\min} = 1.7D$, and corresponding $C_p=0.860$. This value is slightly less than above optimal power outputs, but slightly larger than coagulated optimal array. Difference is in order of 0.1%, so we can conclude that aforementioned three optimal results can be considered as optimal solution.

Table 6 Summary of C_p for 20 subcases of pilot test 2.

$L_y \backslash d_{\min}$	1.5D	2.0D	2.5D	3.0D
370m	0.8552	0.8533	0.8422	0.8240
345m	0.8568	0.8570	0.8401	0.8103
320m	0.8618	0.8613	0.8248	0.8006
295m	0.8645	0.8547	0.8102	0.7856
270m	0.8642	0.8304	0.7884	0.7583

It is also noteworthy to mention that all 20 cases perform better than deploying isolated 8 turbines. The worst optimized array still performs 12.8% better than isolated turbines. Implementing turbines in an isolated way is practically impossible and interaction between turbine are unavoidable. Considering this, all optimized arrays are close to the optimal array for each constraint conditions. In addition, the best array and the worst array's performance shows difference of 14%. It is an interesting result that same number of turbines are optimized in different configurations depending on optimization constraints, and the generated power can be significantly different.

3.4.3 Conclusions of pilot test 2

Through pilot test 2, we came to deduce three major conclusions which provides great intuition to continue with the main test and its aim. Pilot test 2 aimed to observe the impact of d_{min} and L_y on optimization quality. First conclusion is that optimized array

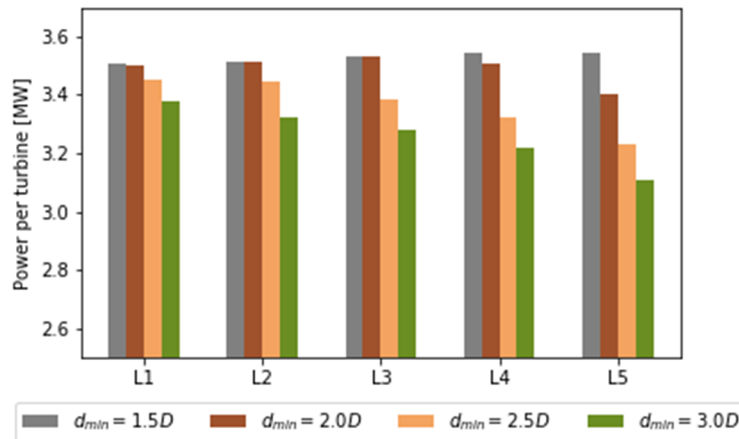


Figure 20 Bar chart of averaged individual turbine power (P_i) for 20 subcases of pilot test 2.

shape is dependent to a non-dimensional number, $\frac{Nd_{\min}}{L_y}$. Second, Among the 20 cases, highest power outputs were obtained from (nearly) uniformly spaced linear barrage type, with a small curvature. Third, all 20 cases perform better than deploying 8 isolated turbines which indicates that V shape condition can be still considered as optimal array configuration, which is less effective.

3.5 Main test: maximum number of turbines which can be considered as a barrage type configuration

From the conclusions of previous thorough research (pilot test 1 and 2) on optimal array configuration, new inspiration was deduced and motivated the topic of the main test. We have previously concluded that uniform linear barrage is efficient optimal array, and when it is not available, curved barrage is considered to be the optimal array. Then a new question arises, that what is the maximum N (N_{\max}) that can be connected as a non-separated barrage shape? Main test aims to answer this question, exploiting PDE-constrained gradient-based optimization with various constraint conditions. Here, N , d_{\min} and L_y are set as variables and initial condition was fixed as arc shape with spacing of d_{\min} .

3.5.1 Simulation settings

Simulation settings for the main is analogous to pilot test 2. It is designed with more caution and attempted to reveal more physical solution. Simulation setting is almost

identical to section 3.2.3 and this is obvious because section 3.2 was designed to tuning simulation parameters which will be used for this pilot test 2 and further the main test. Therefore, only some difference between section 3.2.3 will be described for each sections.

3.5.1.1 Mesh domain

Mesh domain is identical to section 3.2.3.1 because unless the performance of isolated turbine in the pilot test 2 will be different to the one described in section 3.2. Therefore, farm site was fixed as an excessively long length (i.e. 500m) comparing with L_y which was provided as an optimization constraint during the optimization process.

3.4.1.2 Boundary conditions

Boundary conditions used in pilot test 2 is exactly identical to section 3.2.3.2. Therefore, there will be no need for further discussion on this part and it is rather recommended to look section 3.2.3.2 for detailed contents.

3.4.1.3 Parameter settings

Parameter settings used in pilot test 2 is exactly identical to section 3.2.3.3. Therefore, there will be no need for further discussion on this part and it is rather recommended to look section 3.2.3.3 for detailed contents.

3.4.1.4 Test cases

Main test aims to observe the compound effect of N , d_{\min} and L_y on optimization result, and furthermore find the relationship between optimization constraints and N_{max} . Thus, now all variables are changed except for L_x . L_x was fixed as 320m and only L_y was varied as 3 values: (1) 230 m, (2) 300 m, (3) 370 m. Also d_{\min} was varied as 3 values: (1) 1.5D, (2) 2.0D, (3) 2.5D (i.e. 30m, 40m, 50m). N was varied case-dependently. For

each case, N_{start} was determined as the maximum number of turbine which can be linearly spaced with interspacing of d_{min} within L_y . N_{max} was determined through experiments, where some part of turbines are no longer connected to the main part of array.

Initial condition was selected as arc shape, and this was motivated from the conclusion of pilot test 1 and 2. To recall, linear barrage with slight curvature was the optimal array configuration when affordable space in spanwise direction exists within the farm site. From this sense, arc initial condition was provided for all cases. Distance between adjacent turbine was forced to be d_{min} because optimized result does not show significant change when initial condition was given as sparse configuration. This result lies on the fact that turbine by turbine interaction is reduced with sparse configuration and its symmetricity makes initial condition as local optima (or saddle point). For this reason, initial condition was provided as compact as possible, while remaining arc shape which fully spans the L_y . Adequate curvature of arc for each cases were calculated by trial-and-error method.

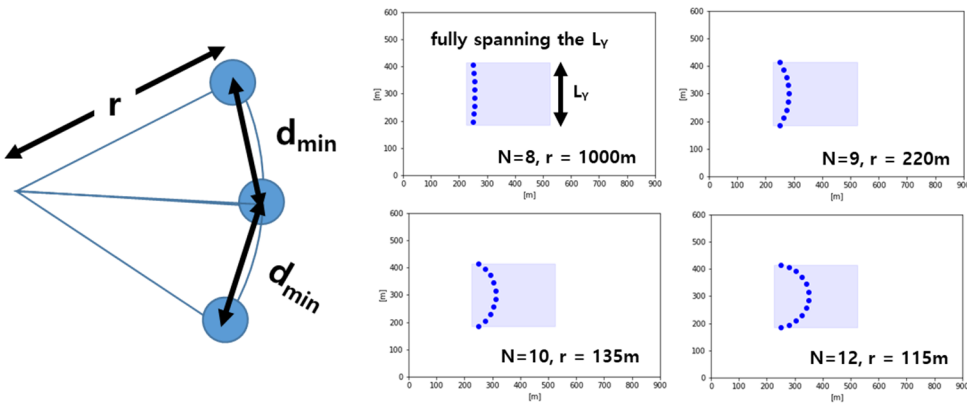


Figure 21 (left) Schematic figure of arc initial condition. Lowercase r is the radius of curvature, and turbines maintain interspacing of d_{min} . (right) Part of initial conditions for $L_y = 230\text{m}$ and $d_{\text{min}} = 1.5D$

Table 7 Definition of case and its corresponding range of N in the main test. In total 70 cases are optimized.

case	L_Y	d_{min}	N_{start}	N_{end}
1	230	1.5D	8	13
2	230	2.0D	6	13
3	230	2.5D	5	11
4	300	1.5D	10	16
5	300	2.0D	8	16
6	300	2.5D	6	15
7	370	1.5D	12	18
8	370	2.0D	9	16
9	370	2.5D	8	15

Chapter 4. Results and Discussions

4.1 Analysis on optimal array configuration and tidal farm output

First, analogous to the pilot tests, optimization result of main test was analyzed to find out the generalized shape of optimal array. To realize this, the total 70 cases were ungrouped and regrouped with N regardless to the d_{\min} and L_y . Because range of N for each case was determined to be the optimized configuration for each initial condition was analyzed by grouping. Optimized results with initially setting uniform arrays (fully-spanned and partially-spanned) did not change from initial condition at all. Intra-spacing in fully-spanned uniform arrays has tuned slightly (to a locally congregating shape), but the general shape remained as fully-spanned linear barrage. Partially-spanned uniform array has not changed from initial condition; it remained with the possible minimal spacing between each turbine which is $1.5D$ (30m). Also, optimization for V-shape initial condition terminated with unchanged shape, with reduced y-direction spacing and unchanged x-direction spacing. It is expected that the aforementioned result is due to the feature of velocity field when actuator disc exists, described in figure 15 (a) and figure 25. Having a

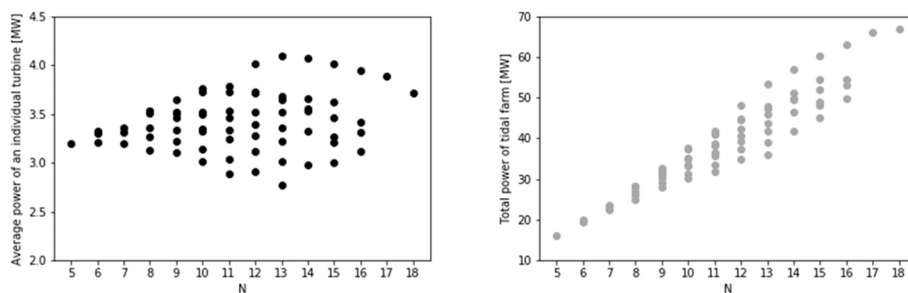


Figure 22 (left) plot of averaged individual turbine power (P_i) for all cases. (right) plot of total farm power output (P_t) for all cases.

longer streamwise spacing is favorable for turbines because flow velocity is more recovered, leading unchanged x-directional spacing during optimization. For spanwise spacing, likewise, it would be better for turbines to be located at where the flow is high-speed. This logic tunes the y-direction spacing in order to locate a turbine behind a turbine at the bypass flow. Aforementioned results are consistent for different number of implanted turbines.

Table 8 List of maximum and minimum power for each number of turbines.

N	Max	P_i [MW]	Min	P_i [MW]	▲[%]
8	Case1	3.527	Case3	3.121	13.0
9	Case8	3.640	Case3	3.108	17.1
10	Case4	3.763	Case3	3.011	25.0
11	Case4	3.785	Case3	2.880	31.4
12	Case7	4.009	Case2	2.912	37.7
13	Case7	4.096	Case2	2.775	47.5
14	Case7	4.067	Case6	2.980	36.5
15	Case7	4.008	Case6	2.998	33.7
16	Case7	3.941	Case5	3.115	33.7

Table 9 Optimized configuration for each N , maximum and minimum cases corresponding to table 8.

N	Maximum	Minimum
8		
9		
10		
11		
12		

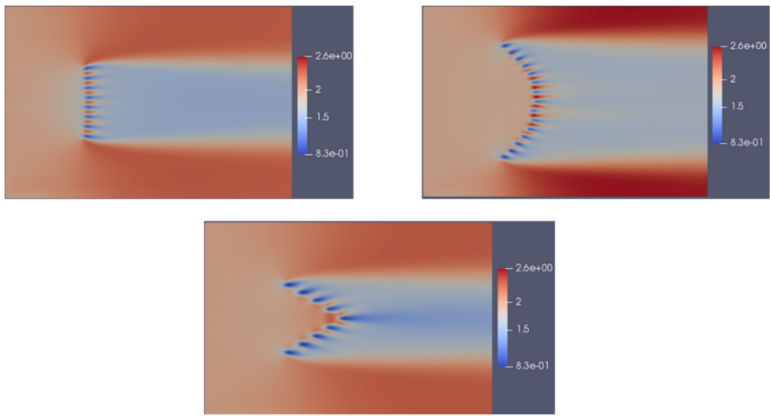
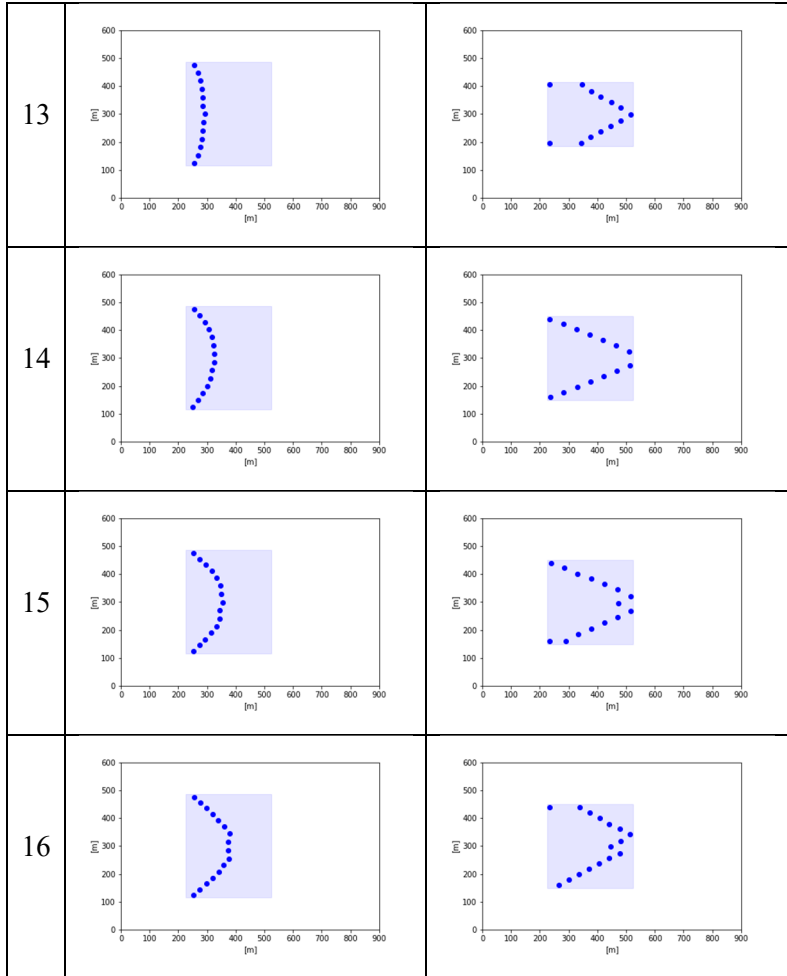


Figure 23 Velocity magnitude field for (upperleft) N=8 case 1, (upperright) N=9 case 3 and (lowercenter) N=15 case 7

In addition, velocity field for N=8 case 1, N=9 case 3 and N=15 case 7 were visualized. These selected results are decent representatives of slightly curved linear barrage, V shape barrage and curved barrage, respectively. It is observed that velocity at the turbine in the slightly curved linear barrage is uniform which indicates that power per individual turbine is also identical for all turbines. For curved barrage, turbine flow velocity is higher for turbines located at the center, thus power per turbine will be non-uniform in this case. V shape shows the slowest turbine flow velocity, which is the reason for the lowest power.

4.2 Extracted Power and N_{max}

For quantified analysis on array performance, average C_T and C_P per one turbine were calculated and compared for all cases. C_T were same for all sub-cases in same number of turbines, indicating that total thrust applied on same number of turbine simulation cases were identical. Results are summarized in table 6. Initial conditions are numbered from 1 to 4, indicating LHS, fully-spanned uniform, partially-spanned uniform, and V-shape, respectively.

As N increases, performance of a single turbine (P_i) reduces. Still it is more efficient than isolated turbine ($P_0 = 2.75MW$). For largest L_Y case (370m), significant performance decline is observed after the N_{max} . This gives adverse effect on the total generated power P_t . For smallest L_Y case (230m), P_i smoothly declines after the N_{max} . For case 6 ($L_Y=(2)$ $d_{min}=(3)$), abnormal decline in P_i is detected at $N=N_{max}$. This is interpreted as, that N_{max} should be 13 not 14 and symmetric and V shape optimized result is actually a

○: N_{max}

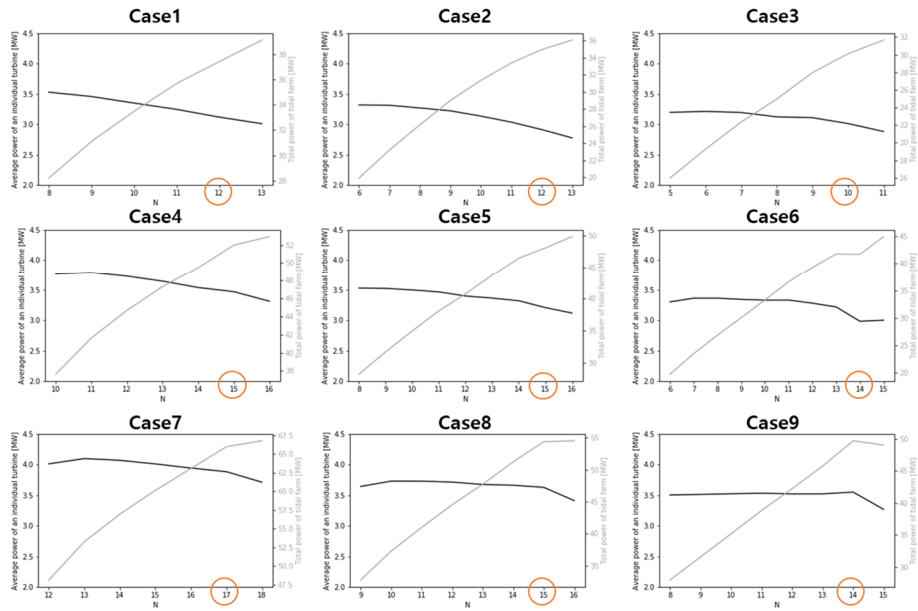


Figure 24 Trend of averaged individual power (P_i , marked in black) and total generated power (P_t , marked in gray) for each cases.

local optimal solution (similar to saddle point).

4.3 Limitations of the Modeling

For some case for optimization constraints, tidal array did not change significantly and this may raise question on the quality of optimization. Thinking of the complexity of the given problem, it is plausible that suggested initial conditions are local optima. Therefore, to check the optimization result is reliable, initial conditions with slightly perturbed from original initial conditions should be applied and tested whether it converges to our intended configurations. Additionally, more initial configurations should be applied, such as staggered array conditions and curved barrage, both tested with fully-spanned and partially-spanned types. It is also suggested to analyze the effect of Froude

number on specific features of optimized array configuration.

Limitations of actuator disc model is very important and may effect highly on practicality on the optimized configurations, especially on the lateral and streamwise spacing issues. Wake issues are critical in wind farm design, and it is natural to extend this issues for tidal turbine. Turbines should be spaced with enough spacing because non-uniform inlet flow gives adverse effect on power output for the turbine behind. Actuator disc, however, cannot account for the performance change due to non-uniform flow and thus optimized result should be modified to secure appropriate spacing in order to implemented for practical design. Also noting that wake effect is not modeled in flow simulation due to large artificial diffusion. However, large momentum diffusivity is inevitable for SWE-coupled optimization because modeling the flow's strong nonlinearity will make it difficult the (local) optimal solution exists. Therefore, it can be concluded that actuator disc modeling is a good choice for the optimization scheme in this study. Spacing issues can be solved by properly imposed inequality constraints during optimization.

Major improvements are also related to the tidal flow modeling. Providing artificial viscosity coefficient as a large constant value can be considered as zero-equation model. It would be a better flow simulation if turbulence model is included, but as mentioned in above paragraph, simplified flow modeling is indispensable for stable optimization. Yet, modeling will be more realistic if the artificial viscosity coefficient is applied differently for the area behind the turbine, where strong wake effect exists and thus momentum diffusion is active. Moreover, improvements on boundary condition on the wall is suggested. First, free-slip boundary condition cannot model a realistic narrow

channel. This study used free-slip boundary condition which was one of the assumptions for LMADT derivation, but this condition would be more proper to model a tidal farm implemented in large ocean with no geographical barriers near around. Note that free-slip boundary condition can be improved by periodic boundary conditions for aforementioned case. For channel modeling, strong Dirichlet condition (i.e. velocity is zero on the wall) will be more adequate instead. Expected result would be different to this study; turbine will move far from the wall because the flow is slow near the wall.

Still, this study provides intuition on channel hydrodynamics with turbine implemented inside. Engineering simplification was necessary for PDE-coupled optimization, and this study can be evaluated as reasonable approach to find the near-optimal configuration of tidal farm in shallow water regions.

Chapter 5. Conclusions

This study aimed to find the near-optima array configurations of tidal stream farm in order to extract high power as possible at an idealized channel. Due to the fact that tidal flow is predictable and strongly governed by hydrodynamic governing equations, PDE-constrained gradient-based optimization was selected as optimization scheme. Governing PDE was selected as SWE with large artificial viscosity coefficient in order to assure convergence of optimization. Target functional was total generated power and turbine positions was set as controls. Channel was modeled as uniform rectangular cross-sectioned channel with constant bed friction, with the Froude number near 0.1.

Turbine was modeled as actuator disc which models the thrust on the water body which is proportional to the local flow velocity square. Turbine friction coefficient K was set as 10 in order to model the wake structure similar to real turbine cases and was set as constant for the case of same number of turbines. Since gradient-based optimization includes computing derivative of friction function during the computation process of the derivative of target functional, friction function should be continuous. Therefore, friction function was modeled as a bump function over a thin rectangular strip to compromise between the continuous friction function over the domain and disc-like shape of turbine in actuator disc model.

Boundary conditions for inlet and outlet velocity was given as Ffether boundary condition and surface level perturbation was clamped as zero for the outlet. Before

conducting main test, two pilot tests were conveyed to provide useful insight for designing main test. Throughout the pilot tests, it was observed that optimal turbine positions are highly affected by initial array configuration and V-shape initial condition tends to converge to the most efficient array layout after optimization. In addition, among the optimal array, the most effective optimal array layout was, even though sensitive to optimization constraints (i.e. L_y and d_{\min}), able to be generalized as a shape of linear barrage with small curvature or a left-pointed V-shape barrage (i.e., \sphericalangle).

Based on the conclusions of pilot tests, main test was conducted in order to observe the change in optimal array configuration as varying number of implemented turbines under different optimization constraints. Initial array configuration was set as arc, which is a compromise between linear barrage and V-shape barrage. As number of turbine increases, curvature of optimal array layout increases, and later the array becomes V-shape and further breaks down into a main barrage and some single turbines.

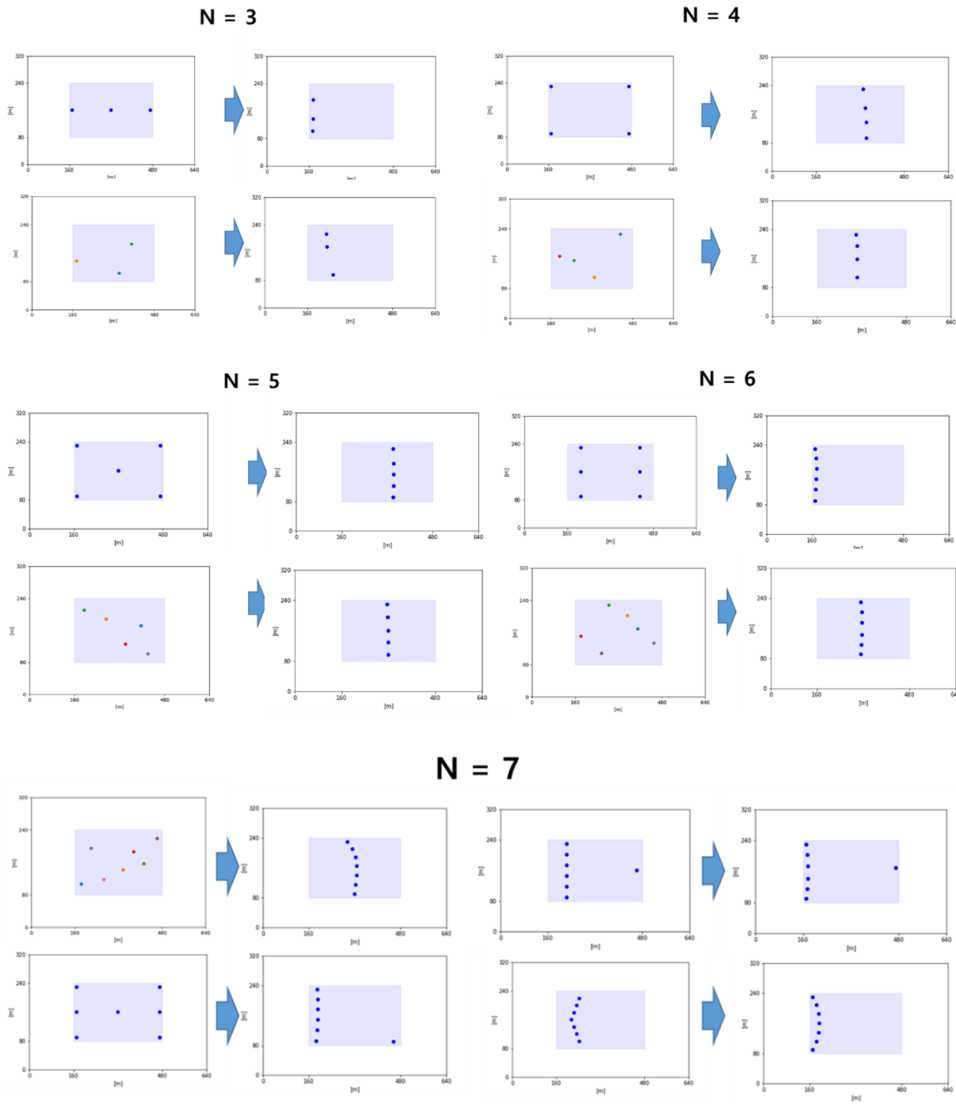
It was found that optimization result is highly dependent on d_{\min} and L_y , and also sensitive to initial condition. Thus, it is recommended to use proper initial condition which resembles optimal array configurations. Analysis on the various case of optimized result (over 100 cases) suggests that linear barrage with uniform spacing can be considered as acceptable optimal array. Furthermore, if linear barrage shape is impossible due to the optimization constraints (such as d_{\min} and L_y), it was observed that connecting all turbines as a curved or V shaped barrage performs better than splitting the array into two parts.

This study highlights the necessity of designing proper site constraints and distance constraints, showing that the performance of optimal array for identical N can vary up to 50% with different constraints. It is expected that this optimal shape of array can be implemented for array design in tidal energy resource assessment or for recommended initial condition in gradient-based optimization.

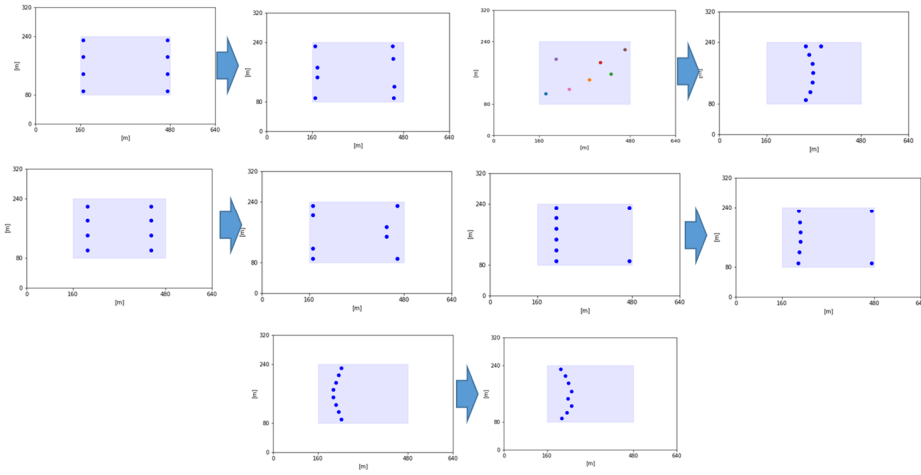
APPENDIXS

Appendix A.

Graphical results of Pilot Test 1

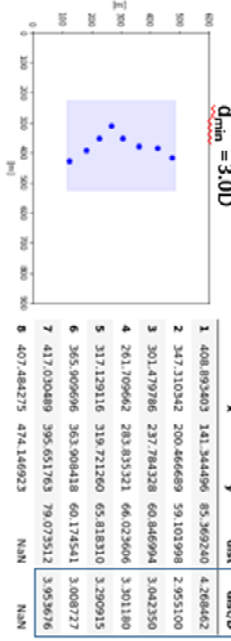
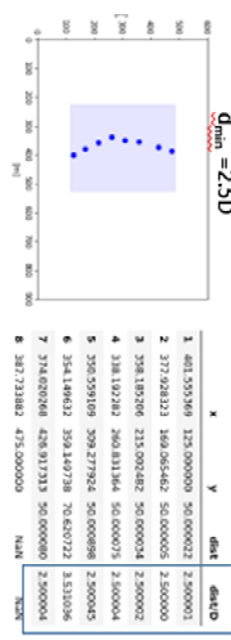
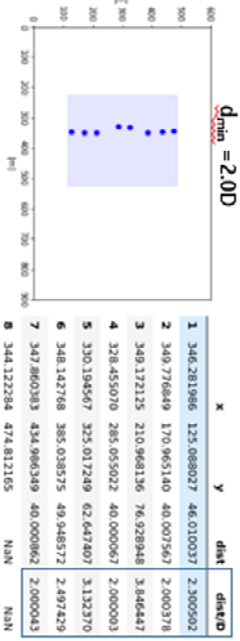
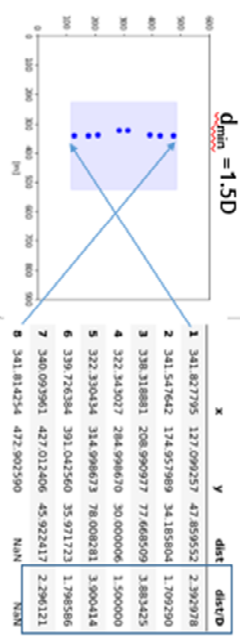


N = 8



$L_y = (1) \ 370m$

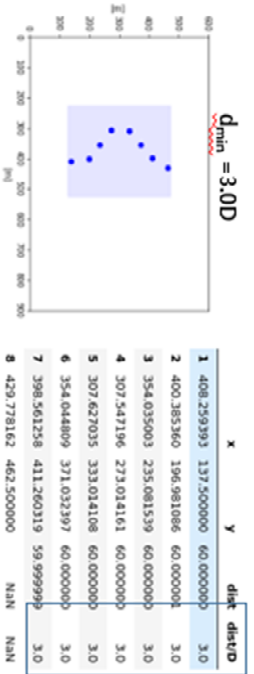
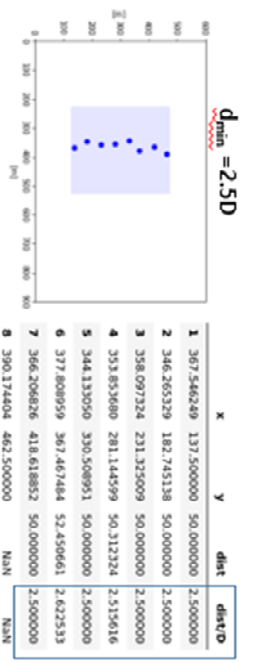
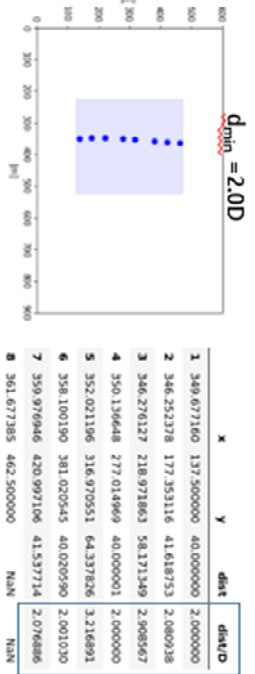
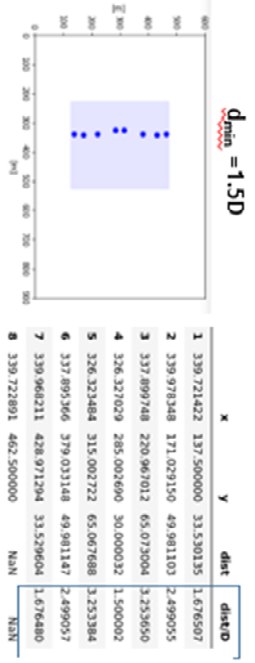
	coef	C_p	min_dist			
			1.5	2.0	2.5	3.0
0						
1	0.855248	0.853339	0.842167	0.824028		
2	0.856792	0.857033	0.840105	0.810329		
3	0.861820	0.861268	0.824778	0.800621		
4	0.864490	0.854713	0.810202	0.785562		
5	0.864205	0.830447	0.788361	0.758330		



Appendix B.

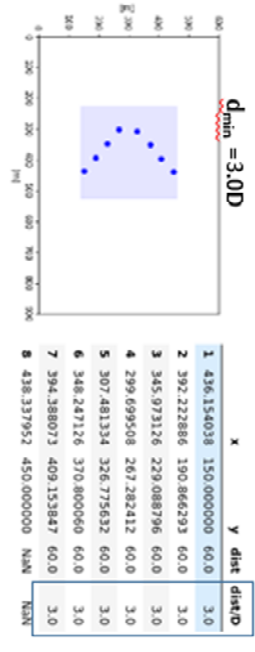
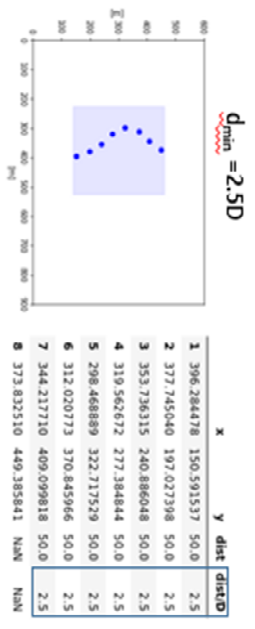
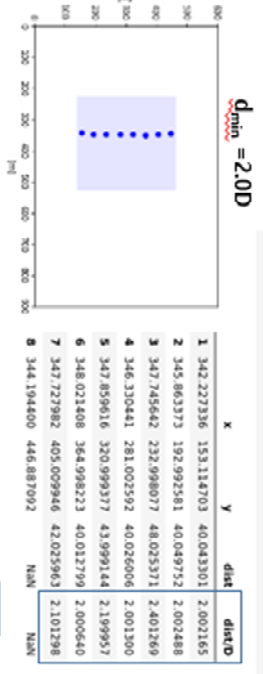
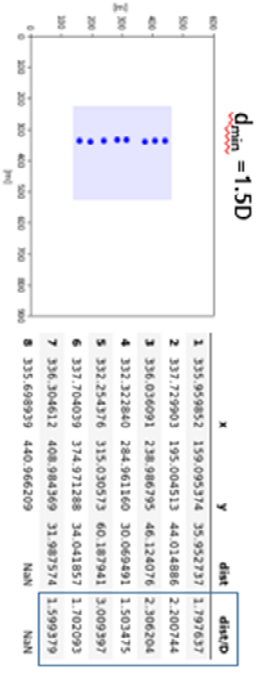
$L_y = (2) \ 345m$

coef	C_p	2.0	2.5	3.0	
8	1	0.855248	0.853339	0.842167	0.824028
	2	0.856792	0.857033	0.840105	0.810329
	3	0.861820	0.861268	0.824778	0.800621
	4	0.864490	0.854713	0.810202	0.785562
	5	0.864205	0.830447	0.788361	0.758330



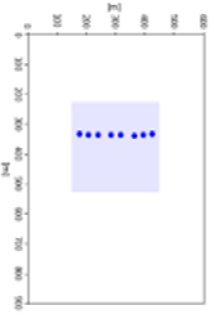
$L_y = (3) \ 320m$

	coef	C_p	1.5	2.0	2.5	3.0
1	0.855248	0.853339	0.842167	0.824028		
2	0.856792	0.857033	0.840105	0.810329		
3	0.861820	0.861268	0.824778	0.800621		
4	0.864490	0.854713	0.810202	0.785562		
5	0.864205	0.830447	0.788361	0.758330		



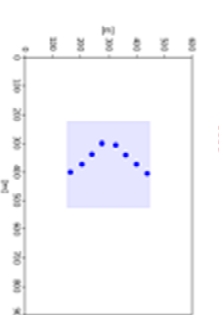
$L_y = (4) \text{ 295m}$

$d_{min} = 1.5D$



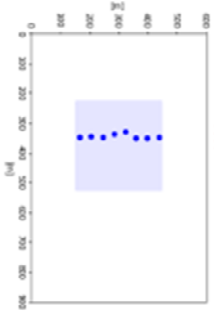
	x	y	dist	distD
1	333.865077	176.973979	30.103537	1.505177
2	335.774749	207.016883	32.063633	1.602182
3	336.198900	239.077711	43.912208	2.195615
4	336.215014	282.990016	34.026794	1.701340
5	336.284135	317.016740	45.919591	2.295980
6	337.729849	362.913567	32.123144	1.606157
7	336.044566	394.992557	30.099350	1.504967
B	333.941629	423.018242	NAN	NAN

$d_{min} = 2.5D$



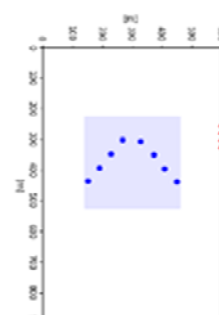
	x	y	dist	distD
1	399.597322	162.669750	50.0	2.5
2	372.512175	204.698250	50.0	2.5
3	338.074160	240.947707	50.0	2.5
4	301.648785	275.199398	50.0	2.5
5	307.645172	324.837200	50.0	2.5
6	342.109190	361.061466	50.0	2.5
7	372.352925	400.874499	50.0	2.5
B	406.396117	437.500000	NAN	NAN

$d_{min} = 2.0D$



	x	y	dist	distD
1	347.606081	164.852094	40.000000	2.0
2	344.343374	204.718807	40.000000	2.0
3	346.069529	244.681544	40.000000	2.0
4	335.817851	283.365521	40.000001	2.0
5	328.224447	322.618162	40.000000	2.0
6	348.208616	357.268313	40.000001	2.0
7	348.018899	397.267864	40.000000	2.0
B	347.786201	437.267187	NAN	NAN

$d_{min} = 3.0D$

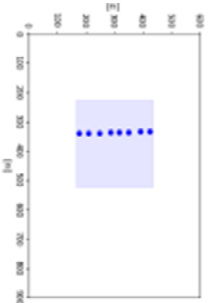


	x	y	dist	distD
1	441.475942	162.502161	60.0	3.0
2	393.867268	199.018105	60.0	3.0
3	345.765309	234.881758	60.0	3.0
4	296.432802	269.032947	60.0	3.0
5	300.393356	328.902074	60.0	3.0
6	349.614872	363.213277	60.0	3.0
7	396.326335	400.870189	60.0	3.0
B	443.847456	437.500000	NAN	NAN

	coef	C.P	1.5	2.0	2.5	3.0
1	0.855248	0.853339	0.842167	0.824028		
2	0.856792	0.857033	0.8440105	0.810329		
3	0.861820	0.861268	0.824778	0.800621		
4	0.864490	0.854713	0.810202	0.785562		
5	0.864205	0.830447	0.788361	0.758330		

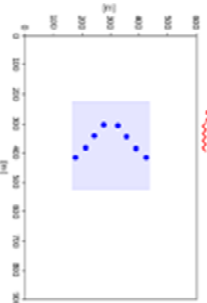
$L_y = (5) \ 270m$

$d_{min} = 1.5D$



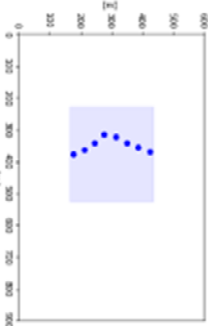
	x	y	dist	distD
1	337.703139	175.065381	33.944775	1.697239
2	338.164985	209.607015	39.947239	1.997362
3	337.957507	248.953715	37.975219	1.898763
4	336.243315	286.890226	30.160904	1.508025
5	336.023590	317.048929	32.055082	1.602754
6	335.846857	349.104524	41.941957	2.097098
7	334.150484	393.021161	33.966718	1.698336
8	332.026239	424.932889	NAN	NAN

$d_{min} = 2.5D$



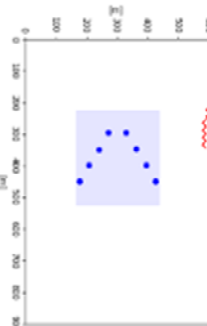
	x	y	dist	distD
1	415.393844	175.000000	50.0	2.5
2	380.368997	210.682770	50.0	2.5
3	342.263763	243.055462	50.0	2.5
4	303.816904	275.021679	50.0	2.5
5	306.384953	324.955687	50.0	2.5
6	345.007219	356.709630	50.0	2.5
7	384.359416	387.554603	50.0	2.5
8	417.493119	425.000000	NAN	NAN

$d_{min} = 2.0D$



	x	y	dist	distD
1	376.570322	175.000000	40.000002	2.0
2	363.618885	212.862291	40.000001	2.0
3	339.854727	245.037823	40.000001	2.0
4	313.953157	275.519108	40.000001	2.0
5	322.123156	314.675860	40.000001	2.0
6	342.356929	349.180859	40.000000	2.0
7	355.688428	386.893866	40.000000	2.0
8	367.850769	425.000000	NAN	NAN

$d_{min} = 3.0D$



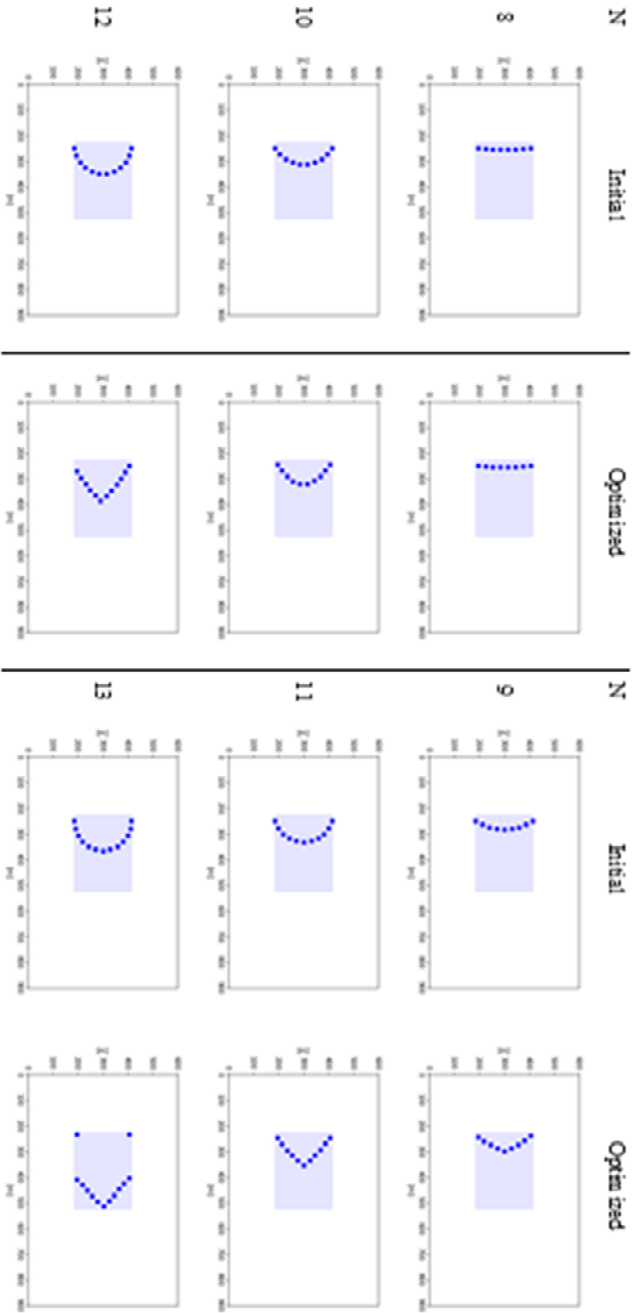
	x	y	dist	distD
1	449.617997	175.000000	60.000001	3.0
2	398.893847	207.047945	60.000000	3.0
3	347.078861	238.791872	60.000000	3.0
4	296.271931	269.143112	60.000004	3.0
5	295.744370	329.141378	60.000001	3.0
6	346.623109	360.973782	60.000004	3.0
7	397.456880	392.848411	60.000001	3.0
8	448.115934	425.000000	NAN	NAN

coef	C_p	1.5	2.0	2.5	3.0
1	0.855248	0.853339	0.842167	0.824028	
2	0.856792	0.857033	0.840105	0.810329	
3	0.861820	0.861268	0.824778	0.800621	
4	0.864490	0.854713	0.810202	0.785562	
5	0.864205	0.830447	0.788361	0.758330	

Appendix C.

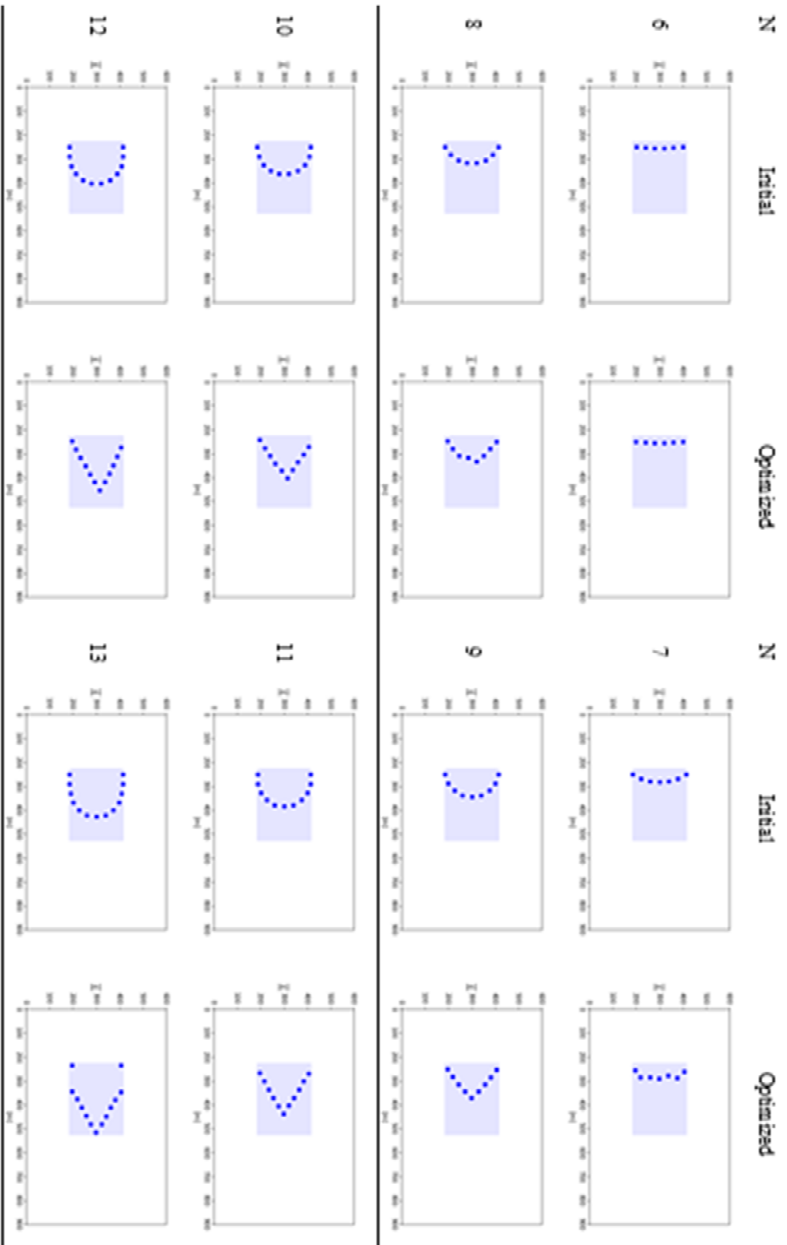
Case1: L_y (1) d_{min} (1)

L_y : [(1) 230, (2) 300, (3) 370]m
 d_{min} : [(1) 1.5D, (2) 2.0D, (3) 2.5D]



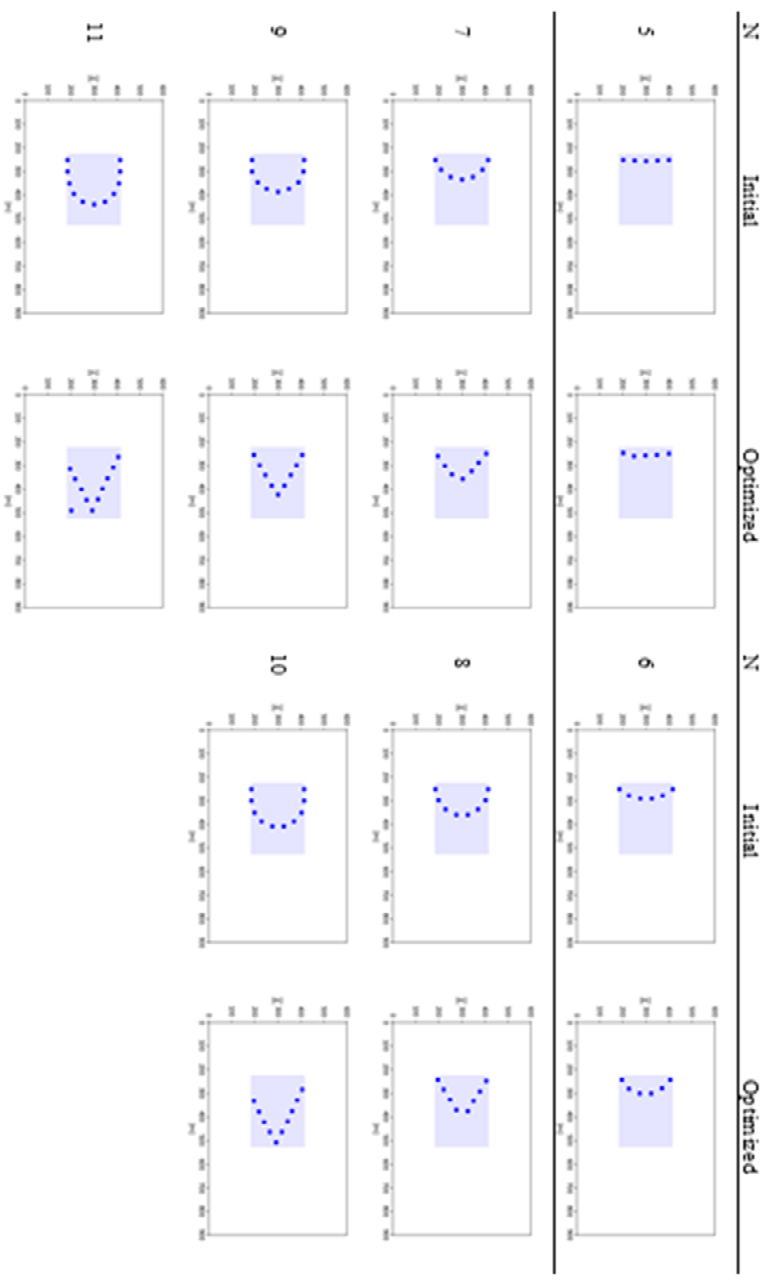
Case2: L_y (1) d_{min} (2)

L_y : [(1) 230, (2) 300, (3) 370]m
 d_{min} : [(1) 1.5D, (2) 2.0D, (3) 2.5D]



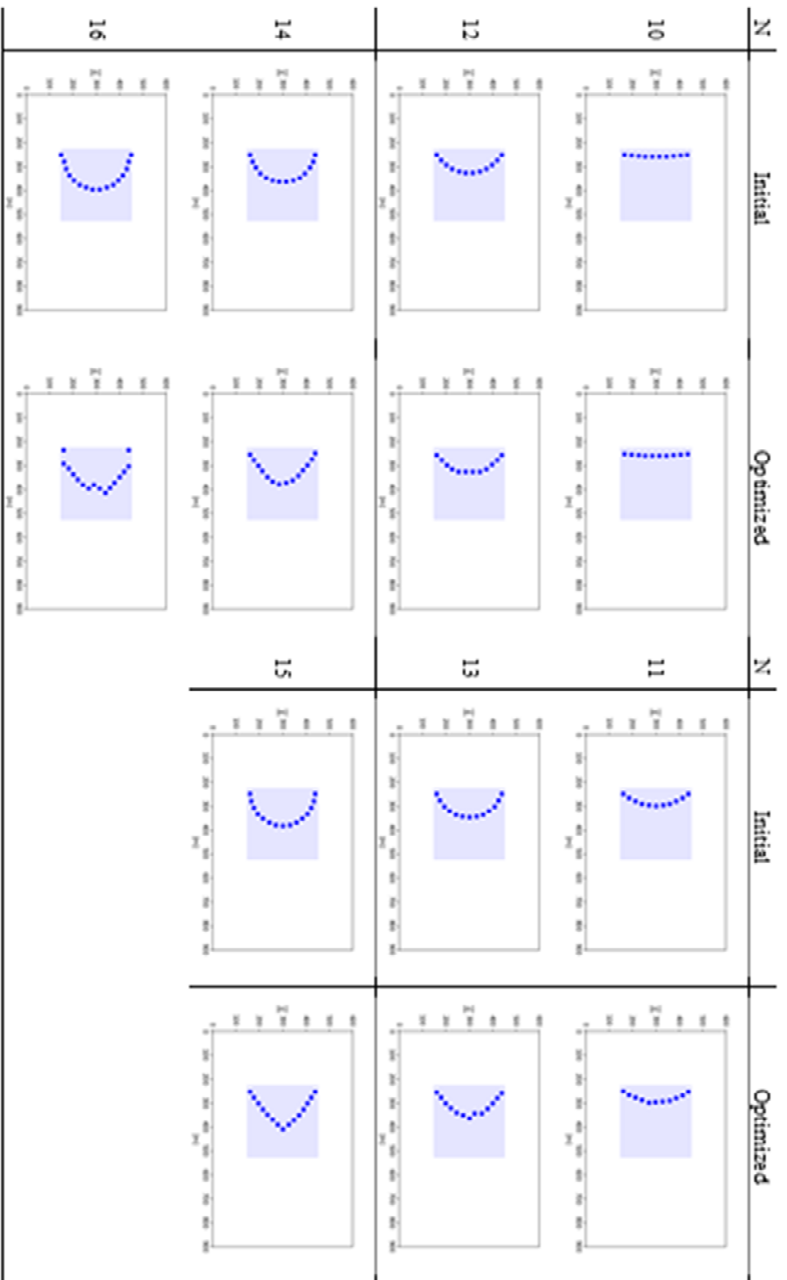
Case3: L_y (1) d_{min} (3)

L_y : [(1) 230, (2) 300, (3) 370]m
 d_{min} : [(1) 1.5D, (2) 2.0D, (3) 2.5D]

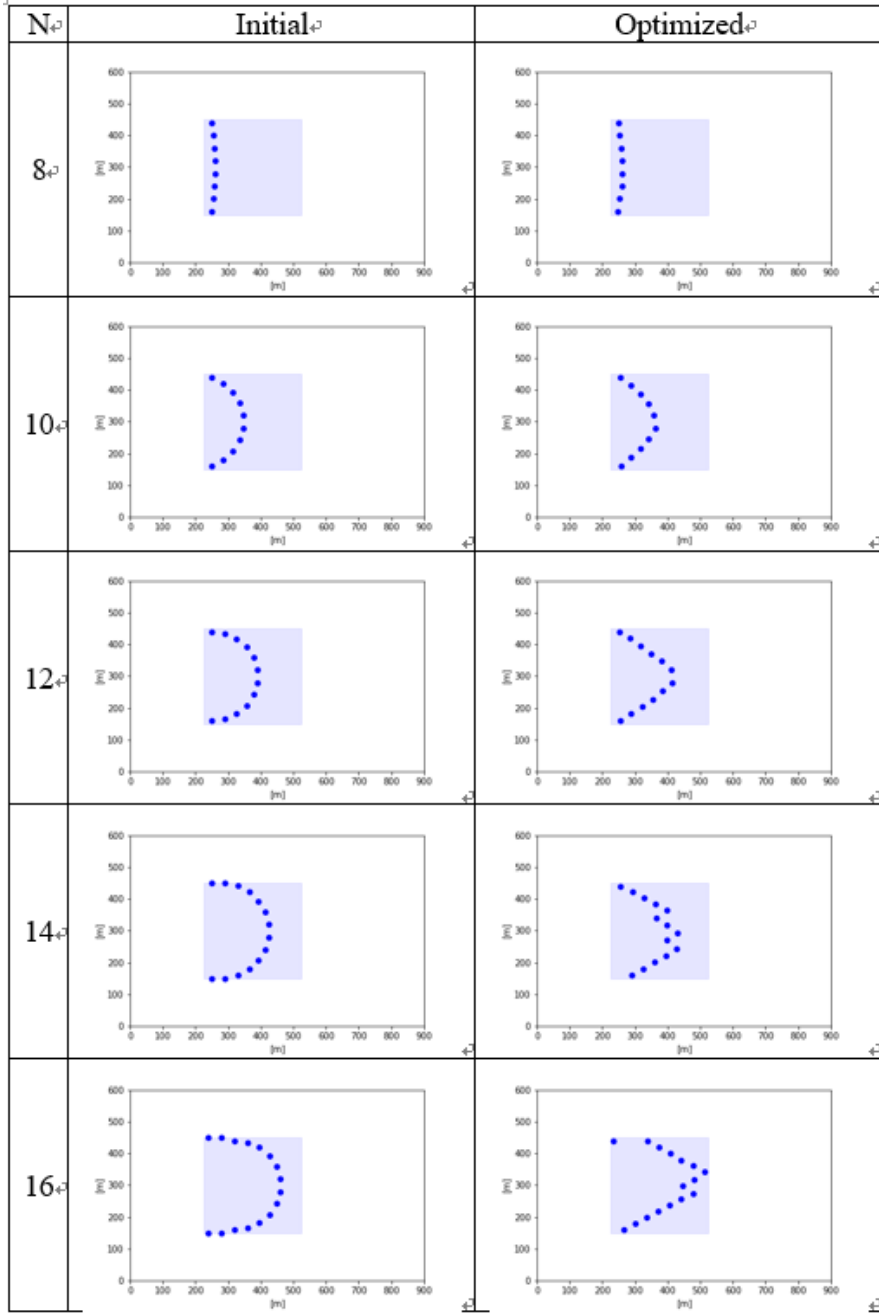


Case4: L_y (2) d_{min} (1)

L_y : [(1) 230, (2) 300, (3) 370]m
 d_{min} : [(1) 1.5D, (2) 2.0D, (3) 2.5D]



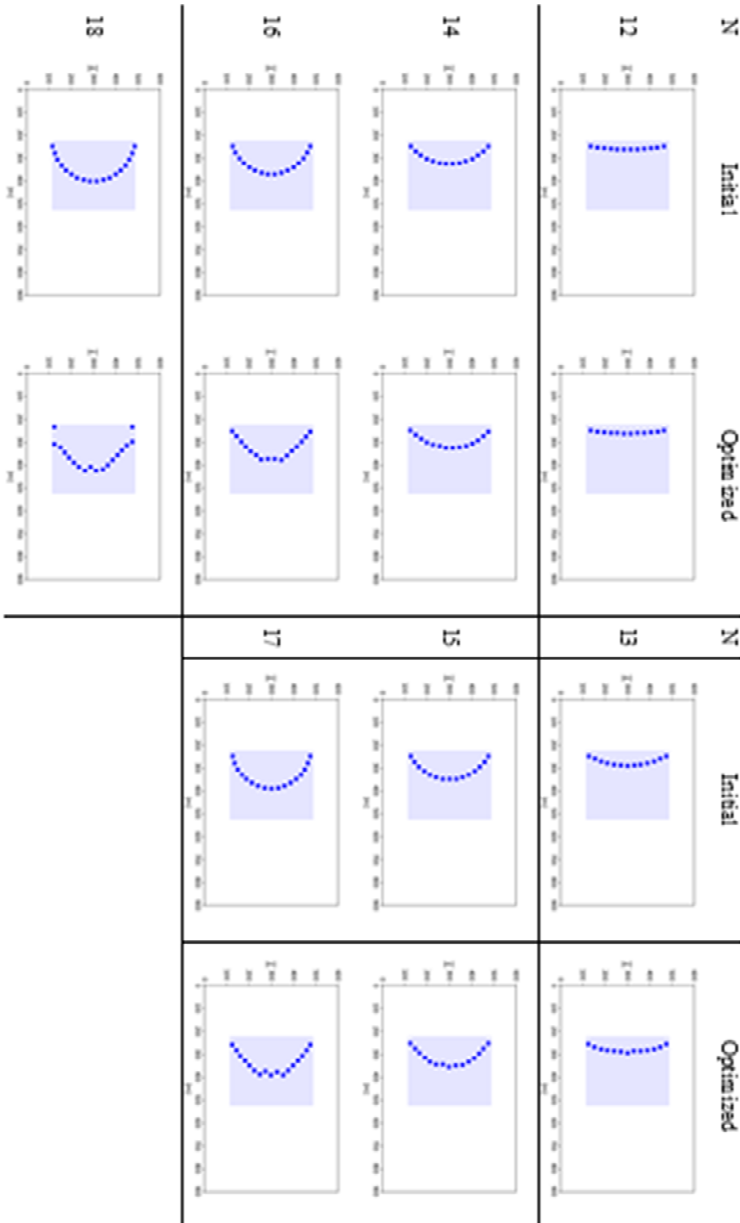
Case5



Case7: L_y (3) d_{min} (1)

L_y : [(1) 230, (2) 300, (3) 370]m

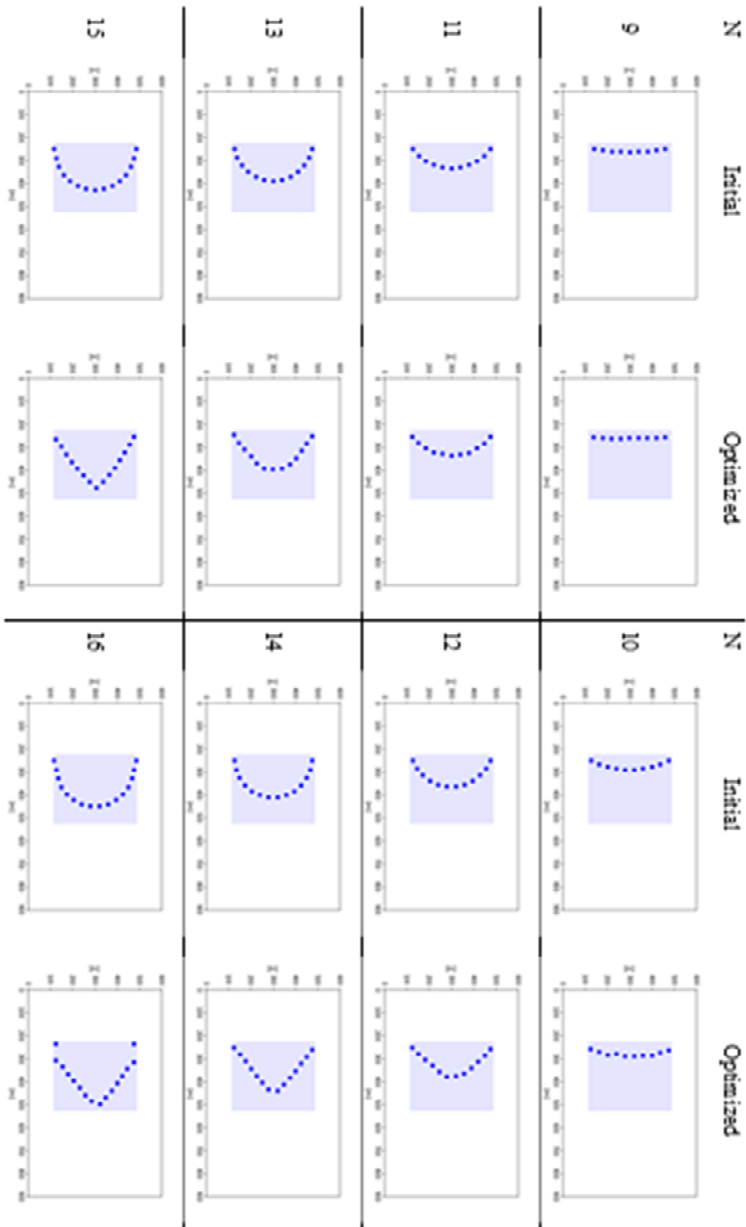
d_{min} : [(1) 1.5D, (2) 2.0D, (3) 2.5D]



L_y : [(1) 230, (2) 300, (3) 370]m

Case8: L_y (3) d_{min} (2)

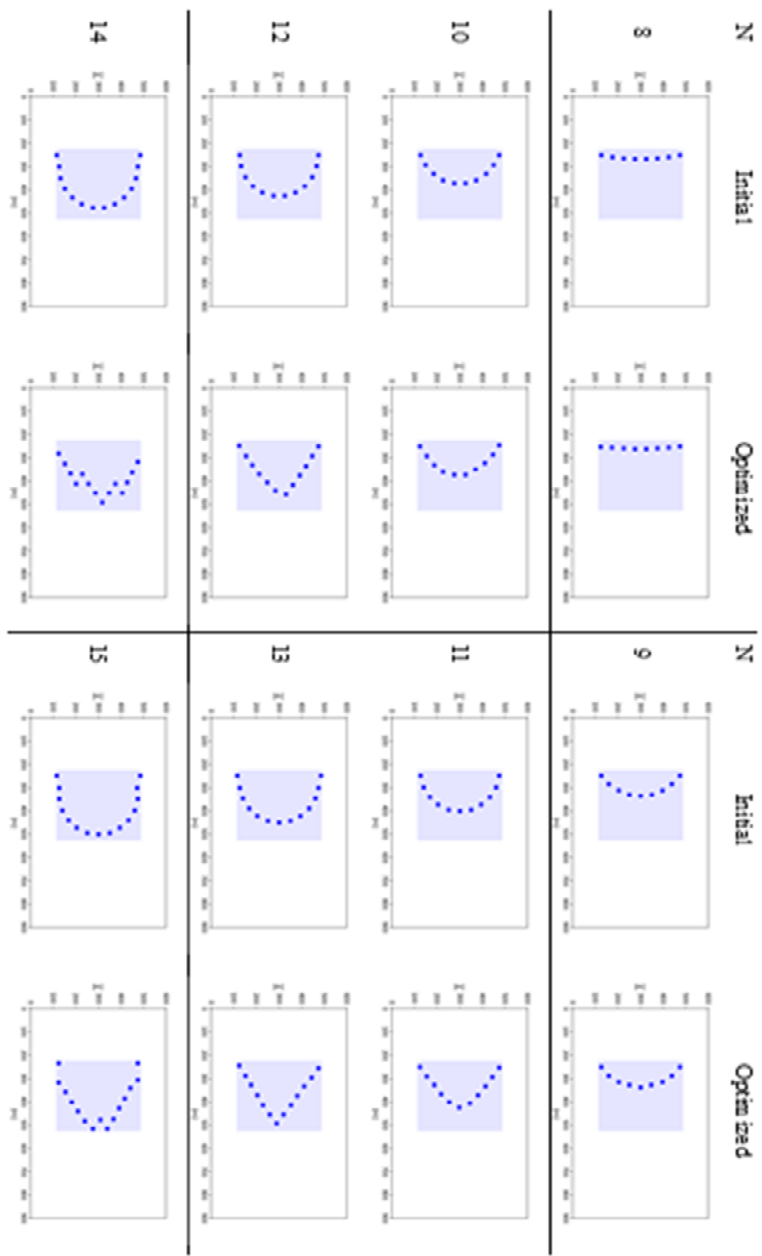
d_{min} : [(1) 1.5D, (2) 2.0D, (3) 2.5D]



L_y : [(1) 230, (2) 300, (3) 370]m

Case9: L_y (3) d_{min} (3)

d_{min} : [(1) 1.5D, (2) 2.0D, (3) 2.5D]



REFERENCES

- [1] Adcock, T. A., Draper, S., & Nishino, T. (2015). Tidal power generation—a review of hydrodynamic modelling.
- [2] Bonar, P. A., Adcock, T. A., Venugopal, V., & Borthwick, A. G. (2018). Performance of non-uniform tidal turbine arrays in uniform flow. *Journal of Ocean Engineering and Marine Energy*, 4(3), 231-241.
- [3] Burton, T., Sharpe, D., Jenkins, N., Bossanyi, E. (2001). *Wind Energy Handbook*. John Wiley & Sons, Ltd. West Sussex, England.
- [4] Carter, G. S., & Merrifield, M. A. (2007). Open boundary conditions for regional tidal simulations. *Ocean Modelling*, 18(3-4), 194-209.
- [5] Churchfield M.J., Li Y. & Moriarty P.J. (2013). A large-eddy simulation study of wake propagation and power production in an array of tidal-current turbines.
- [6] Culley, D. M., Funke, S. W., Kramer, S. C., & Piggott, M. D. (2016). Integration of cost modelling within the micro-siting design optimisation of tidal turbine arrays. *Renewable Energy*, 85, 215-227.
- [7] Denny, E. (2009). The economics of tidal energy. *Energy Policy*, 37(5), 1914-1924.
- [8] Draper, S. (2011). Tidal stream energy extraction in coastal basins. Univ. Oxford, DPhil Thesis, 253.

- [9] Flather, R. A. (1976). A tidal model of the northwest European continental shelf, *Memoires de la Société Royale des Sciences de Liège*, 10, 141–164.
- [10] Funke, S. W., Farrell, P. E., & Piggott, M. D. (2014). Tidal turbine array optimisation using the adjoint approach. *Renewable Energy*, 63, 658-673.
- [11] Garrett, C., & Cummins, P. (2005). The power potential of tidal currents in channels. In *Proceedings of the Royal Society of London A: Mathematical, Physical and Engineering Sciences* (Vol. 461, No. 2060, pp. 2563-2572). The Royal Society.
- [12] Garrett, C., & Cummins, P. (2007). The efficiency of a turbine in a tidal channel. *Journal of fluid mechanics*, 588, 243-251.
- [13] Gupta, V., & Young, A. M. (2017). A one-dimensional model for tidal array design based on three-scale dynamics. *Journal of Fluid Mechanics*, 825, 651-676.
- [14] Harrison M. E., Batten W. M. J., Myers L.E. & Bahaj A.S. (2010). Comparison between CFD simulations and experiments for predicting the far wake of horizontal axis tidal turbines. *IET Renewable Power Generation*. Vol. 4, Iss. 6, pp. 613-627.
- [15] Hinze M, Pinnau R, Ulbrich M, Ulbrich S. (2009). Optimization with PDE constraints in *Mathematical modelling: theory and applications*, vol. 23. Berlin, Heidelberg, New York: Springer-Verlag; 20
- [16] Houlby, G. T., Draper, S., & Oldfield, M. L. G. (2008). Application of linear momentum actuator disc theory to open channel flow.

- [17] IRENA. (2014). Tidal Energy: 6-15.
- [18] Jacobs C. T. & Piggott M. D. (2015). Firedrake-Fluids v0.1: numerical modelling of shallow water flows using an automated solution framework. *Geosci. Model Dev.*, 8, 533-547.
- [19] Kennedy, J. (2011). Particle swarm optimization. In *Encyclopedia of machine learning* (pp. 760-766). Springer US.
- [20] Lee, K. S., Park, J. S., & Yum, K. D. Development of Tidal Current Power Generation System in Uldolmok. In *Proceedings of the Korean Society for Noise and Vibration Engineering Conference*. The Korean Society for Noise and Vibration Engineering.
- [21] Lee, S. H., Lee, S. H., Jang, K., Lee, J., & Hur, N. (2010). A numerical study for the optimal arrangement of ocean current turbine generators in the ocean current power parks. *Current Applied Physics*, 10(2), S137-S141.
- [22] Myers, L. E., & Bahaj, A. S. (2010). Experimental analysis of the flow field around horizontal axis tidal turbines by use of scale mesh disk rotor simulators. *Ocean engineering*, 37(2-3), 218-227.
- [23] Nishino, T., & Willden, R. H. (2012). The efficiency of an array of tidal turbines partially blocking a wide channel. *Journal of Fluid Mechanics*, 708, 596-606.
- [24] Nishino, T., & Willden, R. H. (2013). Two-scale dynamics of flow past a partial cross-stream array of tidal turbines. *Journal of Fluid Mechanics*, 730, 220-244.
- [25] Park J.S., Lee K.S., Ko J.H., Yi J.H., & Ko D.H. (2017). Introduction on Planning for

Establishment of Sea Test-bed for Tidal Current Energy Converters in Korea, KSCE magazine, 65, 64-70.

[26] Roberts A., Thomas B., Swell P., Khan Z., Balmain S. & Gillman J. (2016). Current tidal power technologies and their suitability for applications in coastal and marine areas, J. Ocean. Eng. Mar. Energy 2:227-245

[27] Salcedo-Sanz, S., Saavedra-Moreno, B., Paniagua-Tineo, A., Prieto, L., & Portilla-Figueras, A. (2011). A review of recent evolutionary computation-based techniques in wind turbines layout optimization problems. Open Computer Science, 1(1), 101-107.

[28] Stallard T., Collings R., Feng T. & Whelan J. (2013). Interactions between tidal turbine wakes: experimental study of a group of three-bladed rotors. Phil Trans R Soc A 371:20120159.

[29] Sun X., Chick J.P., Bryden I.G. (2007). Laboratory-scale simulation of energy extraction from tidal currents. Renewable Energy, 1267-1274.

[30] Sutherland, G., Foreman, M., & Garrett, C. (2007). Tidal current energy assessment for Johnstone strait, Vancouver Island. Proceedings of the Institution of Mechanical Engineers, Part A: Journal of Power and Energy, 221(2), 147-157.

[31] Turnock S. R., Phillips A. B., Banks J. & Nicholls-Lee R. (2011) Modeling tidal current turbine wakes using a coupled RANS-BEMT approach as a tool for analyzing power capture of arrays of turbines. Ocean Engineering, 38, 1300-1307.

[32] Vennell, R. (2010). Tuning turbines in a tidal channel. Journal of fluid mechanics, 663, 253-267.

- [33] Vennell, R. (2011). Estimating the power potential of tidal currents and the impact of power extraction on flow speeds. *Renewable Energy*, 36(12), 3558-3565.
- [34] Vennell, R. (2012). The energetics of large tidal turbine arrays. *Renewable Energy*, 48, 210-219.
- [35] Vogel, C. R., Houlby, G. T., & Willden, R. H. J. (2016). Effect of free surface deformation on the extractable power of a finite width turbine array. *Renewable Energy*, 88, 317-324.
- [36] Wan, C., Wang, J., Yang, G., & Zhang, X. (2010). Optimal micro-siting of wind farms by particle swarm optimization. In *International Conference in Swarm Intelligence* (pp. 198-205). Springer, Berlin, Heidelberg.

국문초록

액츄에이터 디스크 모델에 기반한 조류발전단지 형상 최적화에 관한 연구

한 지 수

조류에너지는 지속가능한 대체에너지 중에서도 예측가능한 특성으로 인해 각광받고 있다. 조류발전단지는 목표 전력량 확보를 위해 백대 이상의 터빈으로 구성하기 때문에 배열의 최적화가 필수적이다. 비록 실제 조건에서의 최적 배열은 바닥지형 및 제한된 가용 구역 등에 큰 영향을 받으나, 조류에너지 부존량 산정과정에서 사용가능한 정형화된 최적 배열에 관한 연구가 필요한 실정이다. 또한 실제 배열을 설계할 때는 조류발전단지의 특성상 경사도 기반 최적화가 불가피한데, 경사도 기반 최적화의 해는 초기배열조건에 따라 국지 최적해로 수렴할 가능성이 높기 때문에 전역 최적해에 가까운 초기조건을 사용할 필요가 있다.

따라서 본 연구는 여러가지 제한조건에 대하여 2차원 조류발전단지 배열의 정형화된 최적해를 제시하고자 한다. 목적함수인 총 에너지 추출량을 구속하는 편미분 방정식은 2차원 정상상태 천수방정식을 사용하여 조류터빈에 의한 조류 흐름의 비선형적인 변화를 반영할 수 있도록 하였다. 천수방정식 솔버와 최적화

를 커플링하는 프로그램으로는 파이썬 기반 오픈소스 소프트웨어인 OpenTidalFarm을 사용하였다. 조류터빈은 액츄에이터 디스크로써 모델링 하였고, 다양한 선행연구에서 제시한 후류의 유속 변화를 가장 비슷하게 모의하는 미정 계수들의 조합을 찾아 조류 모델링에 사용하였다. 다변수 함수의 경사도 기반 최적화는 전역 최댓값이 아닌 초기조건에 따라 다른 국지 극댓값으로 수렴하기 때문에 이상화 된 조류해협에 다양한 초기배열조건을 적용해 여러 국지 최적해 중 가장 출력량이 높은 배열의 형태를 찾았다.

수치모의 결과 가능하다면 가용영역의 폭 전체에 걸쳐 등간격으로 배치된 선형 보 형태의 배열이 최적형태로 나타났다. 하지만 터빈간 최소간격 조건과 가용영역 폭 등의 제한조건들에 의해 위와 같은 배열이 불가능하다면 곡률을 갖는 보 형태나, 더 나아가 V 형 보 형태의 배열이 최적형태로 나타났다. 이는 터빈 배열이 조류를 폭방향으로 가로막는 형태가 효율적이라는 것을 의미하며, 산출가능한 에너지를 계산한 결과 같은 개수의 터빈을 서로 영향을 주지 않도록 독립적으로 배치했을 때 얻을 수 있는 에너지보다 최대 30% 이상 효율적이다. 또한 같은 개수의 터빈의 최적배열이 조력발전단지 설계시 제한조건 (터빈간의 최소 간격, 가용 구역의 폭 제한 등)에 의해 에너지 출력량이 최대 50%까지 차이가 발생할 수 있음을 확인하였다.

이러한 결과는 효율적인 조력발전단지를 설계하기 위해서는 단순히 각 제한 조건에서의 최적배열을 찾는 문제 뿐만 아니라 적절한 제한조건을 설계하는 문제의 중요성을 제시한다. 본 연구에서 제시한 방법론은 얕은 수역에서 최적해에

가까운 터빈배열을 찾기 위한 합리적인 접근방식이며, 터빈이 설치된 채널의 동역학적 특성에 관한 직관을 제공한다고 평가된다.

핵심단어: 조류발전단지의 최적배열 형상, 경사도 기반 최적화, 수반행렬법, 정상상태 천수방정식, 액츄에이터 디스크 모델

학번: 2017-23008